University of Zurich^{UZH}

High-Resolution RIXS Studies to detect Low Energy Excitations in Ca_2RuO_4

Master Thesis

at

Department of Physics
University of Zurich

written by

Pascal Rothenbühler

pascal.rothenbuehler@uzh.ch

Supervisors:
Prof. Dr. Johan Chang
Karin von Arx

Date:
December 8, 2022

Summary

In this thesis, the behaviour of the antiferromagnetic Mott insulator Ca_2RuO_4 was explored. This material is a transition metal oxide containing strongly correlated electron physics which is considered one of the biggest challenges in modern condensed matter physics. But with complexity, a broad number of exotic and fascinating phenomena arise in such systems, including unconventional superconductivity, colossal magnetoresistance as well as the Mott insulating state present in our material, making them promising subjects for modern research. With this motivation, a combination of X-ray Absorption Spectroscopy (XAS) and high-resolution Resonant Inelastic X-ray Scattering (RIXS) at the oxygen $K-$edge was applied to the sample in order to study low energy excitations in the ruthenium d orbitals over their hybridization to oxygen. These methods basically allow the detection of a big variety of charge-neutral excitations, like phonons, magnons, dd excitations, and charge transfer for example, through the photoelectric effect. The recently improved energy resolution at the I21 beamline of the Diamond Light Source then seems promising to uncover new and fundamental insight concerning the material Ca_2RuO_4. The data presented in this work was acquired at this beamline and were able to resolve low energy excitations around 40, 80, 160, 350 and 750 meV. As a result, the 40 meV excitation, predicted theoretically as well as by inelastic neutron scattering measurements, has been detected for the first time with RIXS and was assigned to inter t_{2g} excitations. A strong momentum dispersion was derived for the 80 meV excitation, which tends to rule out a phononic nature and argues more for a magnetic origin. In addition, a new low energy excitation was detected around 160 meV. For the previously detected 350 meV excitation, a substructure of at least three peaks could be resolved with the improved energy resolution and these were assigned to inter t_{2g} excitations. The comparison to theoretical modelling then provided the derivation of two fundamental parameters, namely the crystal field splitting $\delta = 303 \pm 12$ meV and the spin-orbit coupling $\lambda = 99 \pm 5$ meV while consistently predicting an excitation around 40 meV, supporting the inter t_{2g} nature of these excitations.

Zusammenfassung

In dieser Arbeit wurde das Verhalten des antiferromagnetischen Mott-Isolators Ca_2RuO_4 untersucht. Bei diesem Material handelt es sich um ein Übergangsmetalloxid mit stark korrelierten Elektronen, was als eine der größten Herausforderungen in der modernen Physik der kondensierten Materie gilt. Aufgrund ihrer Komplexität treten in solchen Systemen eine Vielzahl exotischer und faszinierender Phänomene auf, darunter unkonventionelle Supraleitung, kolossaler Magnetowiderstand sowie der in unserem Material vorhandene Mott-Isolationszustand, was sie zu vielversprechenden Objekten für die moderne Forschung macht. Aus dieser Motivation heraus wurde eine Kombination aus Röntgenabsorptionsspektroskopie (XAS) und hochauflösender resonanter unelastischer Röntgenstreuung (RIXS) an der $K-$Kante des Sauerstoffs auf die Probe angewandt, um niederenergetische Anregungen in den d Orbitalen des Rutheniums über deren Hybridisierung mit Sauerstoff zu untersuchen. Diese Methoden ermöglichen grundsätzlich den Nachweis einer großen Vielfalt von ladungsneutralen Anregungen wie zum Beispiel Phononen, Magnonen, dd Anregungen und Ladungstransfer durch den photoelektrischen Effekt. Die kürzlich verbesserte Energieauflösung an der I21-Beamline der Diamant-Lichtquelle scheint vielversprechend, um neue und grundlegende Erkenntnisse über das Material Ca_2RuO_4 zu gewinnen. Die in dieser Arbeit gezeigten Daten wurden an dieser Beamline aufgenommen und waren in der Lage, niederenergetische Anregungen um 40, 80, 160, 350 und 750 meV aufzulösen. Infolgedessen wurde die 40 meV Anregung, die sowohl theoretisch als auch durch Messungen der inelastischen Neutronenstreuung vorhergesagt wurde, zum ersten Mal mit RIXS nachgewiesen und den inter t_{2g} Anregungen zugeordnet. Für die 80 meV Anregung wurde eine starke Impulsdispersion abgeleitet, die eine phononische Natur eher ausschließt und für einen magnetischen Ursprung spricht. Darüber hinaus wurde eine neue niederenergetische Anregung um 160 meV entdeckt. Für die zuvor entdeckte 350 meV Anregung konnte mit der verbesserten Energieauflösung eine Substruktur von mindestens drei Peaks aufgelöst werden, die inter t_{2g} Anregungen zugeordnet wurden. Der Vergleich mit einem theoretischen Modell lieferte dann die Ableitung zweier grundlegender Parameter, nämlich der Kristallfeldaufspaltung $\delta = 303 \pm 12$ meV und der Spin-Bahn-Kopplung $\lambda = 99 \pm 5$ meV, wobei konsistent eine Anregung um 40 meV vorhergesagt wurde, was die inter t_{2g} Natur dieser Anregungen unterstützt.

Contents

1   Introduction

To demonstrate the elusive behaviour of the material Ca_2RuO_4 and the motivation behind this work, a brief introduction is given by discussing strongly correlated electron systems, the single layer calcium ruthenate Ca_2RuO_4 itself as well as previous experiments on this material.

1.1   Strongly Correlated Electron Systems

A fascinating field in condensed matter physics, which is attracting tremendous attention, explores strongly correlated electron systems in transition metal oxides (TMO). In such materials, the d valence electrons can be considered neither free nor localized, implying that current theories such as the band model and the ligand field theory fail to explain their behaviour [1], longing for a new theoretical description. These complex systems are also often accompanied by a big variety of exotic phases, as shown in Figure 1a, so their understanding may be of great benefit to the development of new materials. To demonstrate this, it is convincing to lead the discussion back to the year 1986, when Georg Bednorz and Karl Alex Müller reported unconventional superconductivity in the cuprate (copper oxides) $Ba_xLa_{5-x}Cu_5O_{5(3-y)}$ [2]. The subsequent research on cuprate superconductors then pushed the transition temperature to the present limit of $T_c \sim 133$ K under ambient pressure [3]. For comprehension, superconductivity is a state observed in certain materials below their specific transition temperature where the electric resistance vanishes completely and the magnetic flux is expelled. The BCS[1] theory then states that this behaviour is caused by an attractive phonon mediated interaction for electron pairs in a crystal and successfully reconstructs the full physical phenomenology of conventional superconductors. As powerful as this theory may be, there are several unconventional superconductors such as the cuprates that deviate from the predictions of this model, so that even fundamental properties such as the pairing mechanism, linear resistance, and pseudogap phase are still poorly understood [4]. But unconventional superconductivity is not the only interesting phenomena in strongly correlated electron systems. They may exhibit exotic properties such as Mott insulating phases, spin and orbital orders, colossal magnetoresistance and quantum criticality, making them a promising object for research [5–7]. This big variety of phases and phenomena are present because several physical interactions like spin, charge, lattice and/or orbital interactions are simultaneously active, coming along with comparable energy scales of different contributions.
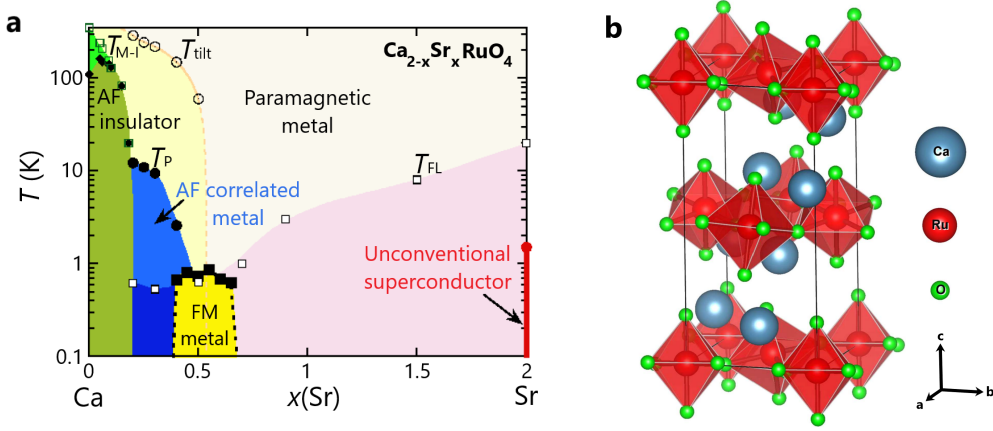
---

[1]Bardeen–Cooper–Schrieffer

Figure 1. (a) Phase diagram of Ca$_{2-x}$Sr$_x$RuO$_4$ depending on temperature T and doping x, taken from [4]. (b) Crystal structure of Ca$_2$RuO$_4$, adapted from [8].

More specifically, this means that even small perturbations may lead to huge changes in the physical properties of the system.

1.2   Single Layered Calcium Ruthenate Ca$_2$RuO$_4$

In this thesis, however, the main focus lies on the layered perovskite Ca$_2$RuO$_4$ which belongs to the class of the ruthenates. Its crystal is built up of corner-sharing RuO$_6$ octahedra compressed along the $c-$axis as depicted in Figure 1b. For the later distinction, the oxygen on the compressed octahedron corners will be addressed as apical oxygen where the remaining will be called planar oxygen. The corresponding lattice parameters are $a \approx 5.36$ Å, $b \approx 5.35$ Å and $c \approx 12.26$ Å, but only above the specific temperature $T_S \sim 360$ K though. At that temperature, a first structural transition happens where cooling causes a metal to Mott insulator transition (MIT) with simultaneous compression along the $c-$axis, resulting in $a \approx 5.39$ Å, $b \approx 5.60$ Å and $c \approx 11.77$ Å [9]. Now, the reason Ca$_2$RuO$_4$ has attracted so much attention recently is exactly that MIT, which can be triggered by hydrostatic pressure [10], temperature [11], chemical substitution [12], epitaxial strain [13], and electrical current [14–16]. Up to this date, the exact mechanism behind this Mott scenario is not fully agreed on. Additionally, powder neutron diffraction has revealed a rotation of the RuO$_6$ octahedra around the $c-$axis and a tilt around an axis in the ab plane [17]. With that information in mind, the crystal above T_S can be associated to the $L - Pbca$ symmetry group where the structure below T_S corresponds to $S - Pbca$ symmetry (L for long and S for short $c-$axis). A further transition occurs at $T_{AF} \sim 110$ K

where the compound turns from a paramagnetic to a G−type antiferromagnetic ordered phase [17–19]. In the latter phase, the magnetic moments are antiferromagnetically aligned in-plane (a, b) as well as in the out-of-plane (c) direction. As usual in TMO, energy contributions compete with each other since spin-orbit coupling λ, crystal field splitting δ, and Hund's coupling J_H are of approximately the same order in the ruthenates [20]. The non-negligible crystal field splits the five otherwise degenerate d orbitals of the ruthenium atom into the threefold degenerated t_{2g} states (d_{xy}, d_{xz}, d_{yz}) and the twofold degenerate e_g states $(d_{z^2}, d_{x^2-y^2})$. The additional compression of the oxygen octahedron along the c−axis implies a further splitting such that the resulting energy levels are d_{xy}, $d_{xz/yz}$, d_{z^2} and $d_{x^2-y^2}$ which are listed with increasing energy. In this octahedral constellation, ruthenium has 4 valence electrons in these d orbitals such that the lowest energy level d_{xy} is fully occupied. The majority spin orbitals d_{xz} and d_{yz} are also occupied [21]. For the spin-orbit coupling on the other hand, it is after many years of research still elusive how strongly it influences the electronic behaviour of Ca_2RuO_4 and also whether it has any impact on the Mott insulating ground state. Spin-orbit coupling leads to level splitting of the d orbitals, so observation of the corresponding excitations in combination with theoretical modelling may reveal the strength of the coupling and its effects on the behaviour of the system. With this intention, various Resonant Inelastic X-ray Scattering (RIXS) studies were performed on this material, whose results will be quickly summarized in the following.

Measurements at the ruthenium L−edge (explained in section 2.2.1) observed excitations at 0.05, 0.32, 0.75, 1, 2.3 and 3.3 eV, where the four excitations lowest in energy were identified as intra−t_{2g} excitations. The remaining two excitations were further determined to correspond to the dd excitations originating from $t_{2g} \rightarrow e_g$ transitions. Due to an energy resolution of $\Delta E \sim 160$ meV however, no dispersive behaviour could have been observed for any of the mentioned excitations [22].
At the Oxygen K−edge (more details in section 2.2.1) on the other hand, excitations were found at 0.35, 2.25 and 4 eV at an energy resolution given by the FWHM ~ 60 meV of the elastic peak. The excitations with energies of 2.25 and 4 eV were then said to be of dd nature whereas the remaining excitation at 350 meV was interpreted and modelled as spin-orbital excitations, yielding a spin-orbit coupling strength $\lambda \sim 200$ meV while predicting an additional excitation around 50 meV [23]. This prognosis actually coincides with data from spin-polarized inelastic neutron scattering measurements [24]. In a more recent study at the oxygen K−edge, excitations around 0.08, 0.4, 1.3 and 2.4 eV could be observed, in addition to the dd excitations corre-

3

sponding to $t_{2g} \rightarrow e_g$ transitions. Also, the 80 and 400 meV excitations have been interpreted as the result of composite spin-orbital excitations where only the latter displayed a small dispersion which was decreasing toward the zone center. Again, theoretical modelling predicts an additional 40 meV excitation that was not detectable due to limited energy resolution [25, 26].

All of these studies have in common that they long for RIXS experiments with improved energy resolution which is crucial to reveal the exact origin of these low energy excitations. Such high resolution measurements have recently become available at the I21 beamline of the Diamond Light Source, where the data presented in this study were collected [27].

1.3 Mott Insulators

Mott insulators are materials that should be metallic conductors according to the band model, but are insulators instead. This behaviour has its origin in the large Coulomb interaction present in strongly correlated electron systems. For illustration, when an electron hops onto a neighbouring site which is already occupied by an electron, it must exert a high energy U to overcome the Coulomb repulsion. If this energy U is much larger than the available kinetic energy t of the electron, the hopping will be strongly suppressed. This then provides the localization of these electrons, manifesting itself in an insulating state. So in a compact notation, a metal turns into a Mott insulator if the condition

$$U \gg t$$

is fulfilled. A theoretical description of this relationship is provided by the so called Hubbard model. This simplistic model describes the behaviour of electrons in a crystal lattice which is assumed to be rigid. Additionally, the interaction between electrons is assumed to be local, meaning that only electrons at the same site interact with each other. The corresponding Hamiltonian, which is composed of the kinetic energy and the interaction energy, is thus given by

$$\mathcal{H}_{\text{Hubbard}} = \mathcal{H}_{\text{kin}} + \mathcal{H}_{\text{int}} = -\sum_{i,j}\sum_{\sigma} t_{ij} c_{i,\sigma}^{\dagger} c_{j,\sigma} + U \sum_{i} n_{i,\uparrow} n_{i,\downarrow}$$

with hopping amplitude t_{ij} between lattice site i and j as well as the local interaction U. The operators $c_{i,\sigma}^{\dagger}$ $(c_{i,\sigma})$ generate (annihilate) an electron with spin σ at the lattice site i. The operator $n_{i,\sigma} = c_{i,\sigma}^{\dagger} c_{i,\sigma}$ is the particle number operator, which specifies the occupation on the site i. Although the Hubbard model looks very simple, the competition between kinetic and
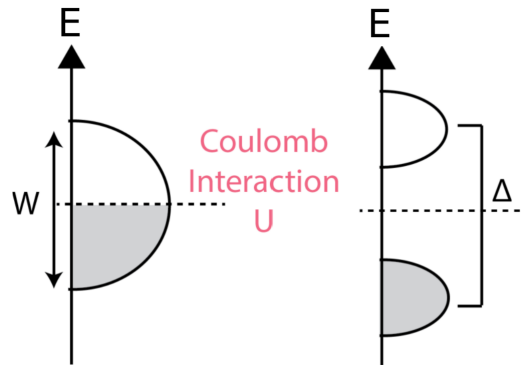
Figure 2. Schematic representation of the density of states for the metal (left) to insulator (right) transition in the Hubbard model, taken from [28]. Strong Coulomb repulsion U splits the band into two Hubbard sub-bands, which are separated by a Mott gap, and turns the material insulating.

potential energy leads to a complex many-body problem, which until today has been solved analytically only for one-dimensional systems [29]. Still, the model is able to successfully describe the metal to insulator transition in this case, as it is illustrated in Figure 2.

However, in the material Ca_2RuO_4, there are three bands, namely d_{xy}, d_{xz}, and d_{yz}, which may be involved in the Mott transition since they all are located near the Fermi energy. One possible scenario could be that the crystal field potential lowers the energy of the d_{xy} band relative to the d_{xz} and d_{yz} bands, turning the material into an insulator.
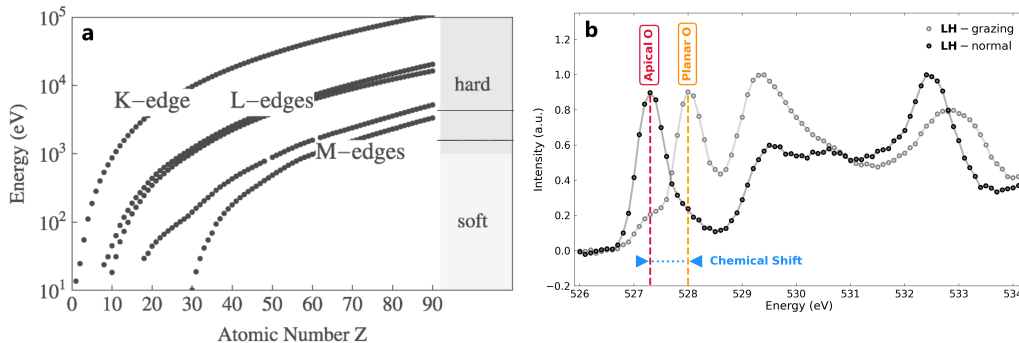
Figure 3. (a) Energy of K, L_1, L_3, M_1 and M_5 absorption edges depending on atomic number Z [30]. (b) XAS spectra of Ca_2RuO_4 to demonstrate chemical shift between absorption edges of apical and planar oxygen.

2   Experimental Methods

To get the most out of the experiments, it is essential to be familiar with the techniques that were used to collect the data. For this reason, both methods, x-ray absorption spectroscopy and resonant inelastic x-ray scattering, are discussed in more detail below as well as the instrumentation of the corresponding measuring device.

2.1   XAS

To improve the cross section of the RIXS process, the incident photon beam is ideally tuned to an absorption resonance specific to the sample.[1] It turned out that X-ray Absorption Spectroscopy (XAS) was very useful in finding these resonances.

2.1.1   Physical Process

The main concept on which XAS is based is the photoelectric effect. The absorption of a photon striking the sample requires a sufficiently high energy such that a bound electron can be promoted from a level deep inside the core to a previously unoccupied state. Consider now a monochromatic x-ray beam hitting the material. While increasing the beam energy, a new absorption channel will become available as soon as the binding energy of an electronic state is reached in the material. As a result, the absorption

---

[1]This absorption resonance is the origin of the R in RIXS

of the photons will peak yielding a so called absorption edge. As the beam energy is further increased, the probability of this transition decreases again and so does the photon absorption until a new absorption edge is reached. The continuation over the whole energy range then yields the characteristic XAS spectrum unique to the material. For comprehension, the $K-$edge corresponds to photon absorption of the $1s$ state whereas the L_1-edge belongs to the $2s$ state and the L_2/L_3-edges to the $2p$ states. So far, it has not been mentioned why it is crucial to examine absorption edges in advance of any RIXS. This has its origin in their sensitivity to environmental changes, manifesting in element and site specific absorption edges. Element specific emphasizes that the energy of the absorption edges are actually increasing with the atomic number of the element under investigation, as depicted in Figure 3a. Site specific on the other hand states that the atomic energy levels and thus these resonances can vary due to the underlying crystal structure, as this changes the binding energy. The site dependence of these edges is present even when chemically different sites are occupied by the same element, resulting in an energy difference known as a chemical shift [20]. For example, in Ca_2RuO_4 we have a chemical shift for the planar and apical oxygen due to the compressed octahedral structure of the ruthenium ligands which can be appreciated in Figure 3b .

There are several options for measuring absorption, and which one is preferable depends on the sample and the further experiments. In the following, two different approaches suitable for RIXS on Ca_2RuO_4 are presented, namely the Total Fluorescence Yield (TFY) and the Total Electron Yield (TEY) mode.

Total Fluorescence Yield

As the name may suggest, TFY mode measures the relaxation radiation of the previously excited core hole excitations. The associated fluorescent photons are then collected by a detector of limited angular extent and then integrated over a broad energy range. Therefore, it is convincing that the measured intensity at the detector, apart from some background noise, is proportional to the absorption in the sample.

Total Electron Yield

In TEY mode, on the other hand, XAS spectra can be acquired by measuring the current from the ground to the sample. Indeed, x-ray absorption may emit photoelectrons, secondary electrons and Auger electrons, which are then
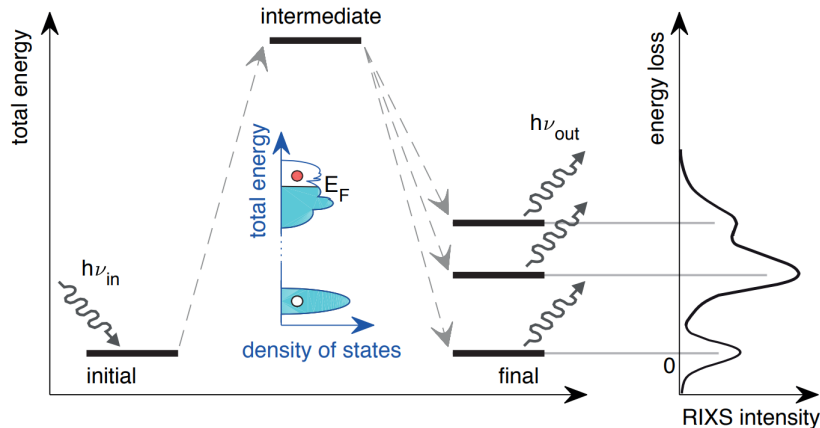
Figure 4. Illustration of the RIXS process. The material absorbs the incoming photon by exciting an electron from deep inside the core into an unoccupied state. This leads to a highly unstable intermediate state such that the system relaxes by emitting another photon. The energy difference between the incoming and outgoing photons then corresponds to the energy transferred to the material in the form of an excitation left behind and results in a typical RIXS spectrum sketched on the right. Figure taken from [20].

replaced from the sample holder. This implies a measurable current proportional to the absorbed intensity, so that the XAS spectra can be reproduced. Even though Ca_2RuO_4 is a Mott insulator, it is still possible to measure such a current by gluing the sample on the holder with silver epoxy which ensures good electric contact.

At this point, it should be mentioned that the TEY mode is more surface sensitive than the TFY mode due to the larger escape depth of photons compared to electrons. Also, all XAS data shown in this work were collected in TFY mode.

2.2 RIXS

Resonant Inelastic X-ray Scattering (RIXS) is a powerful technique which has the ability to detect a big variety of charge-neutral excitations in a broad range of materials. By the stimulation of the sample with photons it is possible to reveal these excitations and their energetic dispersions.

2.2.1 Physical Process

As in XAS, there is a monochromatic x-ray beam incident on the sample, exciting electrons from low energy levels into unoccupied states. This in-
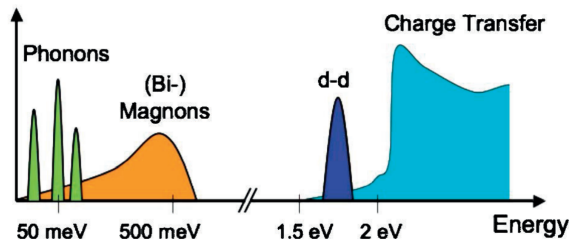
Figure 5. Sketch of the charge-neutral excitations observable with RIXS and their expected energy ranges [30].

termediate state is highly unstable, which is why the system needs to fill the core hole. A possible occupation of this hole could be by the originally excited electron where the energy difference would be compensated by the release of a photon. This process would then be equivalent to elastic scattering, but it does not have to relax in this way. Likewise, electrons from energetically lower levels could fill the hole, which then leads to excitations in the sample. A visualization of the RIXS process just described is shown in Figure 4. Comparing the energy of the incoming and outgoing x-rays, one can determine their energy difference, which is identical to the energy transferred into the system.[1] And this, moreover, corresponds exactly to the energies of present excitations which were intended to be observed. Among those, RIXS is capable of detecting phonons, magnons, *dd* excitations, and charge transfer, to name a few, and these are expected to occur at energies scales illustrated in Figure 5. As briefly mentioned in section 2.1, the incident photon beam is tuned to the relevant absorption resonance to enhance the associated transition. This means that the chemical element in which the absorption is to take place can be well selected. Since in Ca_2RuO_4 the main interest lies in the excitations of the ruthenium *d* electrons we would need to approach the according L_3-edge to generate them. This would require a beam energy of about 2.8 keV, which is exactly between soft and hard x-rays, meaning that its wavelength is too large for the groove spacing of grating monochromators and at the same time too small to match inter-plane spacing in crystal monochromators. Despite major instrumental improvements in recent years that actually enabled RIXS at the ruthenium L_3-edge [22], the energy resolution is still quite limited. Gladly, the ruthenium *d* orbitals hybridize with the neighbouring oxygen *p* orbitals. In this way, we can take advantage of the oxygen $K-$edge by the $O\ 1s \rightarrow O\ 2p$ transition, which only requires an energy of about 530 eV. Even though

---

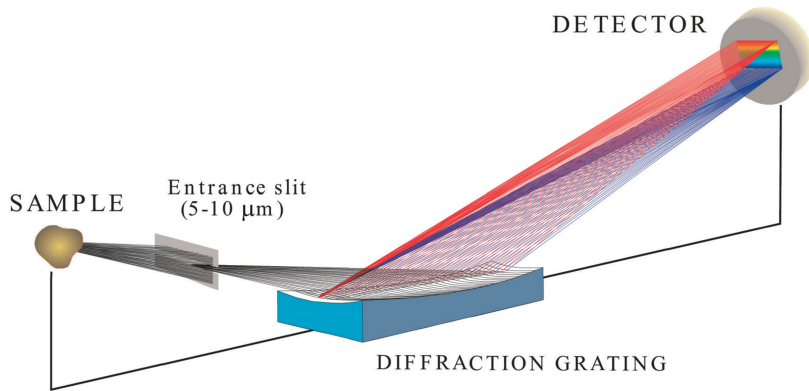[1]This inelastic scattering is the origin of the I in RIXS

Figure 6. Illustration of the RIXS spectrometer, taken from [20].

this transition would be forbidden in free ions, it is accessible in this crystal structure due to the aforementioned hybridization and is ideal for triggering excitations in the related d orbitals [20].

2.2.2 Spectrometer and Preprocessing

The spectrometer is the part of the instrument that is able to resolve the energy loss of the x-ray beam to the sample. It consists of an entrance slit, a diffraction grating and a two-dimensional CCD detector, as shown in Figure 6.

The entrance slit limits the radiation to a small angle to reduce noise caused by scattering from surrounding objects. A reduction of the slit would enhance the energy resolution, but also reduce the photon flux, which then increases the duration of the measurement. So it is always a trade-off between these two quantities. After the slit, the grating scatters the photons of the remaining polychromatic beam, with lower energies causing greater diffraction. This allows the incidence height on the detector to be linked to a specific energy, but also means that tuning the beam energy to a different absorption edge would require an adjustment of the grating and detector geometry. In the end, the photons hit the pixels of the detector and yield an intensity distribution as shown in figure 7a. The entrance slit has a horizontal extension, which means that photons with the same energy can hit the detector at different locations of the same height, giving the typical line-shaped intensity pattern. In practice, however, the alignment of these lines need not be exactly horizontal and can have a finite slope. This may be due to a slight tilt of the slit or grating and must be taken into account when adding the
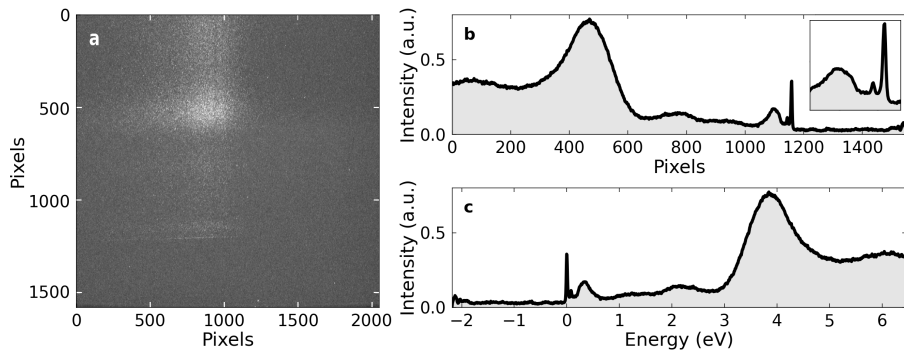
Figure 7. Calibration procedure of a RIXS spectrum, for Ca_2RuO_4 with incident energy of 528.0 eV and linear horizontal light polarization. One can see (a) the measured intensity on the detector, (b) the spectrum from horizontally added intensities and (c) the final RIXS spectrum after converting pixel to energy loss. The inset in (b) is a zoom of the spectrum around the elastic peak.

different vertical spectra of the greyscale map. This addition then results in a single spectrum as shown in Figure 7b and is also briefly elaborated in the Appendix A. Since the probability of a photon gaining energy from the system is negligible and photons with higher energies diffract less, we can identify the lowest line in 7a, which corresponds to the rightmost peak in 7b, with elastic scattering. To convert the pixels into an energy scale, the incident beam energy can be changed such that the elastic peak shifts in pixel. This shift then corresponds to the change in beam energy. However, in materials like Ca_2RuO_4 where low energy excitations are present, this conversion may not be as straightforward, as these excitations could overlap with the elastic peak and distort the resulting energy scale. In such a case, a carbon tape with a clean elastic peak can be placed next to the sample for reference such that one can determine the energy per pixel scale. This tape can additionally be used to determine the energy resolution by evaluating the FWHM of the elastic peak. This width can then be further used to localize the zero energy loss position, since it is only limited by the resolution and should not change within an experiment. By fitting the elastic peak with data from the negative energy loss side (see section 4.1 for details), the exact zero energy loss position can be determined. The scale for energy loss was defined as $E_{in} - E_{out}$ by convention such that excitations are located at positive values [20].
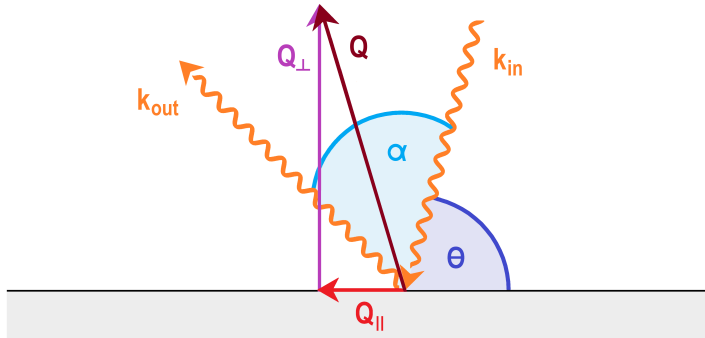
Figure 8. Sketch of momentum conservation with $\mathbf{k}_{\text{in}}$ ($\mathbf{k}_{\text{out}}$) the momentum of the incoming (outgoing) photon and $\mathbf{Q}$ the momentum transferred to the sample which can be split into its parallel $\mathbf{Q}_\parallel$ and perpendicular $\mathbf{Q}_\perp$ contributions. θ is the variable angle between the incoming beam and the surface and α the fixed angle between incoming and outgoing photons.

2.2.3   Dispersion in Momentum

One of the great achievements of RIXS is the ability to derive the momentum dispersion of the excitations by changing the angle θ between the incident beam and the sample surface. The sample has been prepared in such a way that the lattice parameter $\mathbf{c}$ lies normal to the surface as depicted in Figure 9. To simplify the calculations, it is convenient to assume only elastic scattering with $|\mathbf{k}_{\text{in}}| = |\mathbf{k}_{\text{out}}| \equiv k$, which is reasonable since the change of the momentum in its absolute value can be neglected.[2] Furthermore, the total momentum must be conserved, which requires a finite contribution of the sample as shown in Figure 8. This contribution equals the momentum of the excitations Q left behind in the crystal, given by

$$\mathbf{Q} = \mathbf{k}_{\text{out}} - \mathbf{k}_{\text{in}} = k \left(\begin{bmatrix} \cos(\theta + \alpha) \\ \sin(\theta + \alpha) \end{bmatrix} + \begin{bmatrix} \cos(\theta) \\ \sin(\theta) \end{bmatrix} \right) \overset{\text{\tiny AT}}{=} 2k \cos(\alpha/2) \begin{bmatrix} \cos(\theta + \alpha/2) \\ \sin(\theta + \alpha/2) \end{bmatrix}$$

---

[2]The momentum change $\Delta k = k_{\text{in}} - k_{\text{out}}$ of the photons can be derived with

$$\Delta E = E_{\text{in}} - E_{\text{out}} = \hbar c \Delta k \quad \Longrightarrow \quad \Delta k = \frac{1}{\hbar c} \Delta E \approx 5 \cdot 10^{-4} \frac{\Delta E}{1 \, \text{eV}} \, \text{Å}^{-1}$$

The energies of the excitations under examination lie far below $E < 10 \, \text{eV}$, such that the momentum change with $\Delta k < 5 \cdot 10^{-3} \, \text{Å}^{-1}$ is negligible.

where addition theorems were used in the last step. Therefore, the momentum of the observed excitations can be summarized as

$$Q = 2k \cdot \cos{(\alpha/2)}$$
$$Q_{\parallel} = Q \cdot \cos{(\theta + \alpha/2)}$$
$$Q_{\perp} = Q \cdot \sin{(\theta + \alpha/2)}$$

In the present case however, the quantity of interest is the in-plane momentum $Q_{\parallel}$ of the sample because Ca_2RuO_4 is a quasi two-dimensional system where the coupling between layers is weak. This means that the out-of-plane direction can be neglected. At this point it must be emphasized that in all the following experiments, the in-plane momentum dispersions were measured along the $Ru-O$ direction and not $Ru-Ru$. Therefore, it is convenient to adjust the notation accordingly such that the new parameters $\mathbf{a_T}$ and $\mathbf{b_T}$ point along the in-plane $Ru-O$ bond. This means that in real space, the new lattice parameters become $a_T \approx b_T \approx \sqrt{a^2 + b^2}/2 = 3.89\text{Å}$. Furthermore, in the following the momentum is expressed by $\mathbf{Q} = h \cdot \mathbf{a_T^*} + k \cdot \mathbf{b_T^*} + l \cdot \mathbf{c^*}$ where $\mathbf{a_T^*}, \mathbf{b_T^*}, \mathbf{c^*}$ are the corresponding reciprocal lattice vectors of the parameters just introduced. Note that for measurements along the $Ru - O$ direction on the quasi two-dimensional Ca_2RuO_4, only the variable h is further needed to describe relevant changes in the momenta of the observed excitations. Therefore the notation was simplified by expressing momenta in a more compact way, namely by h or $(h, 0)$ in the following.

2.2.4 Orbital Selection

Oxygen $K-$edge RIXS is capable of enhancing transitions into specific orbitals by varying the angle θ and polarization of the incident x-ray beam. Since the occurrence of an excitation may depend strongly on the accessed orbital, it is important to discuss under which conditions certain transitions are favoured. Because this study is at the oxygen $K-$edge, the relevant transitions are the $1s \rightarrow 2p_{x/y/z}$ at the apical and planar oxygen. The $1s$ initial state of the electron is isotropic, so neither polarization nor incidence angle have any effect on the transition probability. This is not the case for the $2p$ final states. The transition probability into a specific p state is enhanced if its orientation is aligned with the oscillating electric field of the incoming beam. As indicated in Figure 9a, it is possible to switch the light polarization between linear vertical (LV), which is perpendicular to the scattering plane, and linear horizontal (LH), which is parallel to the scattering plane. Thus, with the additional adjustment of the angle, the polarization can be aligned to all oxygen p orbitals. Now, to deduce where the excitations occur, it is practical to introduce the d orbitals and how they hybridize. The
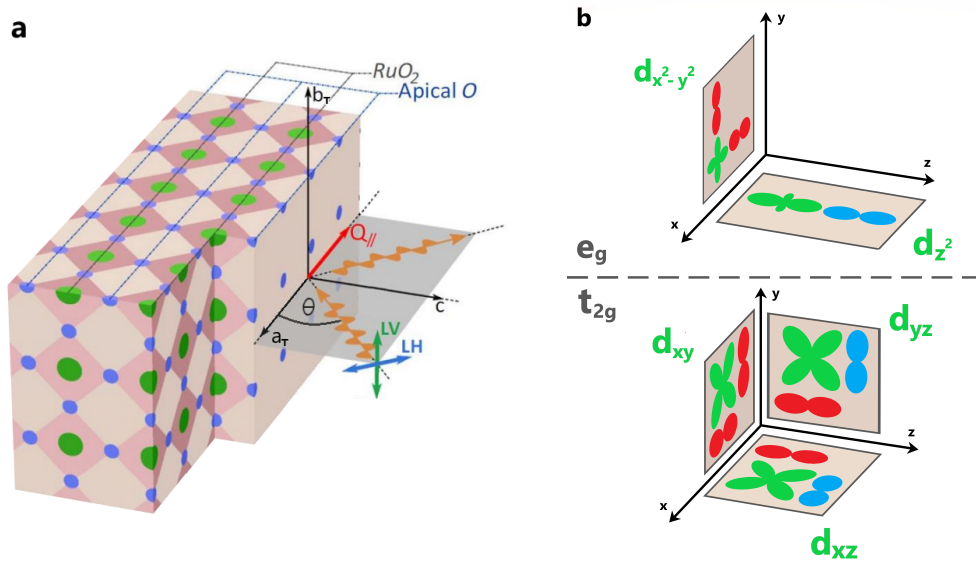
Figure 9. (a) Visualization of RIXS geometry on Ca_2RuO_4, adapted from [25]. Polarization, angle θ and energy of the incoming x-ray beam can be varied to change the in-plane momentum $Q_\parallel$ as well as the orbitals under examination. (b) Selection of ruthenium d orbitals (green) by their hybridization with oxygen p orbitals, where we distinguish between the apical (blue) and planar (red) oxygen. Polarization alignment along the p_x, p_y, or p_z extent then increases the absorption rate of the corresponding orbital. The coordinate systems of both subfigures have been chosen such that they coincide, meaning that the crystal parameters a_T, b_T, and c correspond to x, y and z, respectively.

Ru^{4+} is surrounded by an octahedral crystal field, such that the otherwise fivefold degenerate d states split in two, which will be named the t_{2g} orbitals (d_{xy}, d_{xz}, d_{yz}) at lower and the e_g orbitals ($d_{x^2-y^2}$, d_{z^2}) at higher energy. Note that the x, y, z axes were chosen along the crystal parameters $\mathbf{a_T}, \mathbf{b_T}, \mathbf{c}$, respectively. To be even more precise, the ligand structure is not perfectly octahedral, but compressed along $\mathbf{c}$ such that a further splitting of the e_g and t_{2g} levels occurs. As a result, the d_{xy} state is lowest in energy, followed by a twofold degenerate energy level consisting of d_{xz} and d_{yz}. For the e_g states, the $d_{x^2-y^2}$ is found at higher energies than the d_{z^2} state. To grasp the main hybridization between the e_g and t_{2g} orbitals of ruthenium with the $2p$ orbitals of oxygen, it might be worth taking a look at Figure 9b. However, the lobes of the e_g orbitals point directly to the ligands, so they hybridize with the $2p$ orbitals of oxygen, whose lobes point in the same direction. The lobes of the t_{2g} orbitals on the other hand are oriented along the $Ru - Ru$ direction. They therefore favour hybridization with the $2p$ orbital of oxygen whose lobes are lying in the same plane but diagonal to the ones of the t_{2g} orbitals. Combining now the influence of the beam properties on the choice of a p orbital with their hybridizations, it is possible to observe excitations in a given d orbital by adjusting polarization, angle θ and absorption resonance. For completeness, an overview has been listed in Figure 10 where one can see which d orbital is examined under which conditions.

	Apical Oxygen			Planar Oxygen		
	LV	LH normal	LH grazing	LV	LH normal	LH grazing
p − orbitals	p_y	p_x	p_z	p_y	p_x	p_z
$d_{x^2-y^2}$				**X**	**X**	
d_{z^2}			**X**			
d_{xz}		**X**				**X**
d_{yz}	**X**					**X**
d_{xy}				**X**	**X**	

Figure 10. Overview of the orbital selection. The rows list the various d orbitals (green), while the columns indicate the properties of the incident x-ray beam. An **X** states that the d orbital is observed under the given conditions. Grazing incidence is given for $\theta \rightarrow 0°$ whereas normal incidence corresponds to $\theta \rightarrow 90°$.
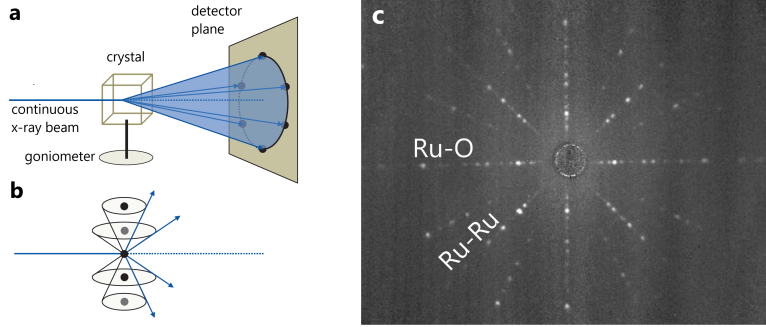
Figure 11. (a) Schematic representation of the Laue process, adapted from [29]. (b) Illustration of the diffraction pattern formation in Laue's process [29]. (c) Laue diffraction pattern of Ca_2RuO_4 in the $a-b$ plane.

2.3 Sample Preparation

For RIXS experiments it is essential to know along which crystallographic axis the measurements are performed. For this purpose, the Laue diffraction method can be used to orient the sample and to detect the desired direction. Consider a polychromatic x-ray beam incident on the sample, as in Figure 11a, with wavelengths comparable to the atomic spacings of the material. If the light is now scattered elastically $|\mathbf{k}| = |\mathbf{k}'|$, the diffracted beam is detectable if the Laue condition

$$\Delta\mathbf{k} \overset{!}{=} h\mathbf{b}_1 + k\mathbf{b}_2 + l\mathbf{b}_3 \quad \Longleftrightarrow \quad \begin{cases} \mathbf{a}_1 \cdot \Delta\mathbf{k} \overset{!}{=} 2\pi h \\ \mathbf{a}_2 \cdot \Delta\mathbf{k} \overset{!}{=} 2\pi k \\ \mathbf{a}_3 \cdot \Delta\mathbf{k} \overset{!}{=} 2\pi l \end{cases}$$

is fulfilled, yielding constructive interference and therefore the typical dots on the detector as in Figure 11c. In the notation of the formula, we have the primitive vectors $\mathbf{a}_i$ of the crystal lattice as well as the scattering vector $\Delta\mathbf{k} \equiv \mathbf{k} - \mathbf{k}'$ which describes the momentum change between the incoming $\mathbf{k}$ and outgoing $\mathbf{k}'$ beam. Also, we have the integer numbers h, k, l which determine in combination with the primitive reciprocal vectors $\mathbf{b}_i$ any point of the reciprocal lattice. So for constructive interference, the scattering vector has to coincide with the distance between any two lattice points in reciprocal space. For visualization, the Laue condition in one dimension is fulfilled for a set of coaxial cones as visualized in Figure 11b. Generalizing then to three dimensions, there are simply three perpendicular sets of coaxial cones whose intersections fulfil the Laue condition and provide the dotted pattern. So if the x-ray beam is incident along an axis of $n-$fold rotation, the radial dotted lines can be associated with high symmetry axes of the perpendicular

crystal plane where the associated point pattern in the detector plane must also have an $n-$fold symmetry [29]. However, care must be taken, as superposition with higher order reflections may occur.

For the orientation of the Ca_2RuO_4 sample though, these first-order reflections can be used to distinguish between the two high symmetry axes along the ruthenium bond to the planar oxygen $Ru - O$ and the $Ru - Ru$ direction. They lie closer to the $Ru - Ru$ axis such that the radial dotted lines on the detector can be assigned accordingly and the orientation of the crystal is given [31].
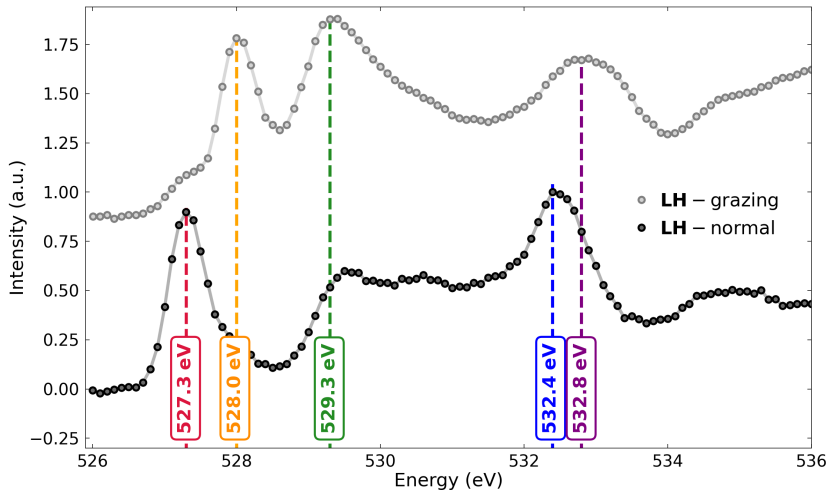
Figure 12. XAS Spectra of Ca_2RuO_4 at normal (black) and grazing (grey) incidence of light with linear horizontal polarization, where the data were collected in TFY mode. Vertical, dashed lines highlight the different absorption edges.

3 Results

In this part of the thesis, the raw data of the measurements are provided and the observations made are discussed objectively. First, the resonances in the XAS spectra are explained, followed by the description of the excitations observed with RIXS and their behaviour under changing conditions.

3.1 XAS

The XAS spectra of Ca_2RuO_4 on the Oxygen $K-$edge have been measured in Total Fluorescence Yield (TFY) mode at $T \sim 15$ K and are presented in Figure 12 with linear horizontal (LH) light polarization for near grazing ($\theta = 15°$) and normal ($\theta = 90°$) incidence. A linear background has been fitted to the intensities below 526.5 eV and was subtracted from the spectra, which were then normalized to the maximum intensity. Clear resonances at energies of 527.3, 528.0, 529.3, 532.4, and 532.8 eV were detected. The lowest two resonances belong to the oxygen $1s \rightarrow 2p$ transition where the p orbitals hybridize with the Ru t_{2g} states. Previous studies have already shown that the absorption at the apical oxygen is at a lower energy than that at the planar oxygen [32, 33], such that they can be assigned to the peaks at 527.3 eV and 528.0 eV accordingly. A detailed assignment can be found in section 5.1. The remaining resonances at higher energies can be connected to the oxygen $1s \rightarrow 2p$ transition where the p orbitals hybridize with the Ru
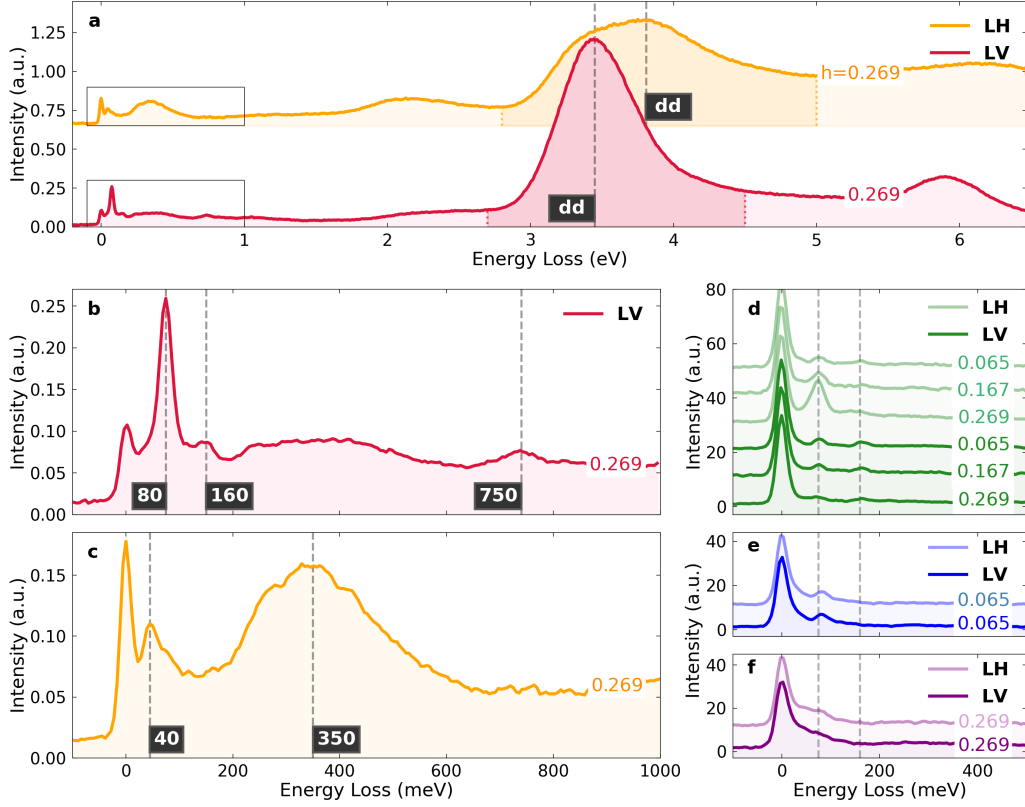
Figure 13. Introduction of excitations. (a) Full range of recorded RIXS spectrum where the dark shaded area has been used for normalization. (b)-(f) Zoom on low energy region of RIXS Spectra at different absorption edges. The colours match the resonances highlighted in Figure 12. The vertical dashed lines correspond to excitations around 40, 80, 160, 350 and 750 meV as well as the *dd* excitations and are guides to the eye.

e_g states. The XAS spectrum for LV polarized light was omitted because it gives nearly the same spectrum as that for LH light at normal incidence. Recall that LV polarization enhances the transition to the planar p_y, which would be almost equivalent to the planar p_x absorption due to the symmetry in the $xy-$plane of the crystal.

3.2 RIXS

Various RIXS spectra were recorded under several conditions to see what kind of low energy excitations exist and how they respond to certain changes. For this reason, the angle between the surface and the incident x-ray beam
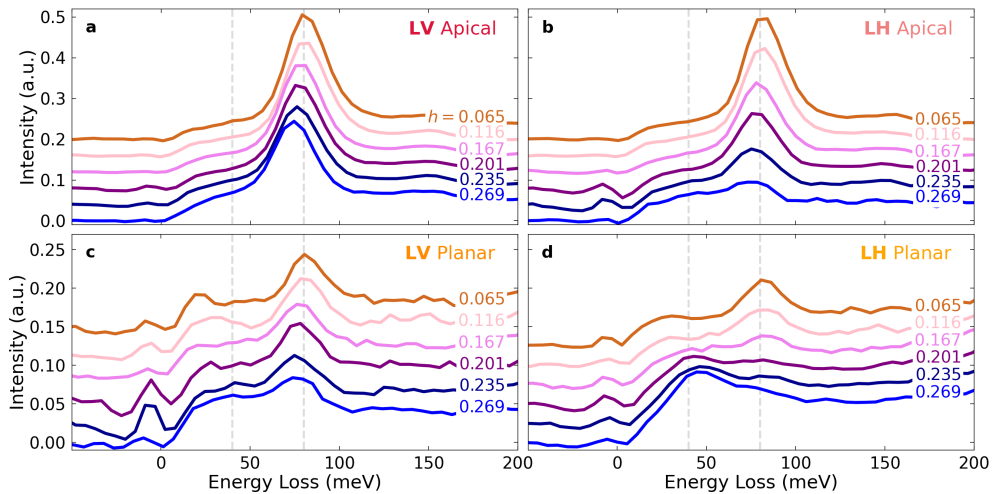
Figure 14. Overview of low energy excitations for (a) LV polarization at apical oxygen edge, (b) LH polarization at apical oxygen edge, (c) LV polarization at planar oxygen edge and (d) LH polarization at planar oxygen edge. The spectra have been shifted vertically for better comparison and the elastic peak has been subtracted. The dashed vertical lines at 40 and 80 meV are guides to the eye.

was changed between $\theta = 20° - 65°$, while the polarization was switched between linear horizontal (LH) and linear vertical (LV) orientation. In addition, different absorption edges were investigated and among them not only the apical and planar oxygen edge but also higher resonances associated to the e_g states. For comprehension, see Figure 12 and 13. The most pronounced excitation at the apical and planar oxygen edge is found at about 4 eV and can be assigned to the *dd* excitations [23, 25]. At lower energies beneath 1 eV though, five distinct excitations at energies around 40, 80, 160, 350 and 750 meV were observed, which are indicated in Figure 13b,c and will be discussed in more detail below. Moreover, the 40 and 160 meV excitations were resolved for the first time in this work and may attract considerable attention.

Generally, the 40 meV excitation is a quite weak feature and therefore hard to detect, especially because the elastic peak in combination with the pronounced 80 meV excitation overlap this feature frequently. Nevertheless, there are certain conditions under which the 40 meV excitation is clearly evident, namely for LH polarized light at the planar oxygen (see Figure 14d and 16c) where the 80 meV excitation is attenuated. At grazing incidence, under which condition the d_{xz} and d_{yz} orbitals are accessed, this feature is most pronounced and weakens slightly with increasing angle θ. Even a small dispersion toward the zone center may be detected by eye and will be further
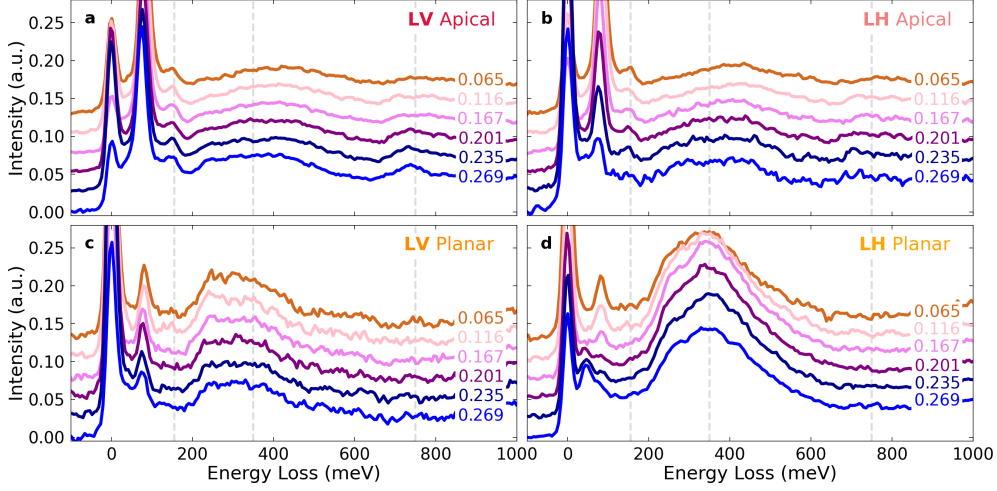
Figure 15. Overview of 350 meV excitations for (a) LV polarization at apical oxygen edge, (b) LH polarization at apical oxygen edge, (c) LV polarization at planar oxygen edge and (d) LH polarization at planar oxygen edge. The spectra have been shifted vertically for better comparison. The dashed vertical lines at 160, 350 and 750 meV are guides to the eye.

elaborated in Section 5.

The 80 meV excitation, which can be appreciated for example in Figure 14a, is well developed at energies corresponding to the apical oxygen edge for LV polarization and LH at normal incidence which correspond to the d_{yz} and d_{xz} orbital, respectively. In the latter case, reducing the angle will be accompanied by a simultaneous decrease of the peak intensity which nearly vanishes at grazing incidence. Though, it was possible to observe dispersions for both polarizations at the apical oxygen edge even by eye, which can be verified in Figure 14a and 14b. The 80 meV excitation energy is maximum in the zone center and decreases with growing in-plane momenta independent of light polarization. At the planar oxygen edge, the peak is rather weak and no dispersion can be discovered. Interesting, however, are the observations when turning to the remaining absorption edges at higher energies. At the 529.3 eV resonance, a similar intensity behaviour of the 80 meV excitation as at the apical oxygen edge was detected. Even for incident photon energies of 532.4 and 532.8 eV, as it is displayed in Figure 13e and 13f, this feature is still identifiable for both polarizations at grazing incidence.

For the 160 meV excitation, exactly the same intensity behaviour can be observed at both the planar and apical oxygen absorption edges as for the 80 meV excitation. More precisely, this means that the peak is absent at the planar but present at the apical oxygen for both polarizations, decreasing
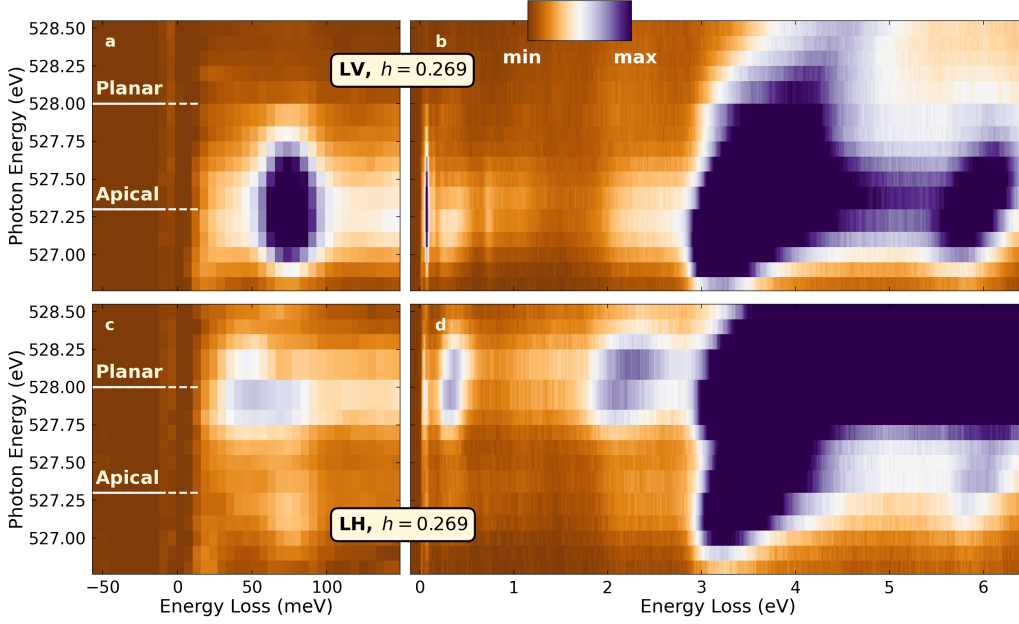
Figure 16. Energy map with (a)−(b) linear vertical and (c)−(d) linear horizontal polarized light at grazing incidence, with the elastic peak subtracted. Note that the left subfigures show a zoom around zero energy loss of the corresponding full spectra on the right in order to highlight the 40 and 80 meV excitations, respectively.

uniformly toward normal LH light incidence. This means that the excitation is present when the d_{yz} and d_{xz} orbitals are accessed. However, at the higher resonances, the 160 meV excitation was only clearly evident at an x-ray energy of 529.3 eV with LV polarization. Still only few in-plane momenta have been probed.

Another quite pronounced feature can be observed at 350 meV energy loss for LH polarized light tuned to the planar oxygen resonance, where LV and LH normal incidence access the $d_{x^2-y^2}$ orbital and LH grazing condition the $d_{xz/yz}$ orbitals. Under these conditions, various angles of incidence θ were measured, finding that the overall intensity of the 350 meV feature barely depends on angle, where its shape does. In some spectra, including the one in Figure 13c, three distinct peaks could be resolved indicating a substructure of multiple (three or more) excitations. The 350 meV feature was barely detected for LV polarization at the planar oxygen absorption edge, as well as at the apical oxygen edge for both polarizations. At the remaining resonances, the 350 meV excitation vanishes under any condition.

For completeness, the weak 750 meV excitation is briefly elaborated, revealed recently in RIXS measurements directly at the ruthenium absorption

edge [22]. This feature occurs only at the apical edge for LV and LH polarization at normal incidence, with the first condition accessing the d_{yz} orbital and the second condition accessing the d_{xz} orbital. Though, the low intensities of this excitation prohibit any further analysis to be established and its behaviour remains unknown.
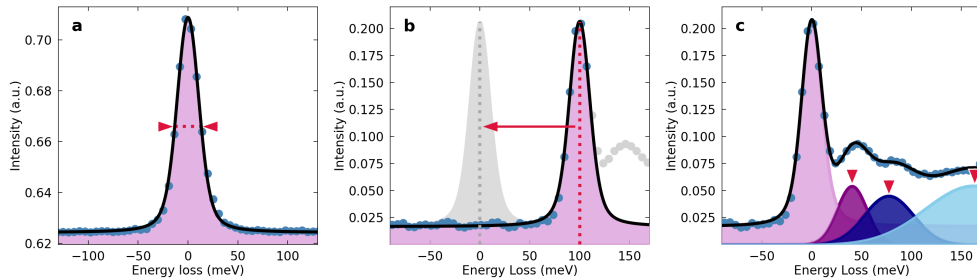
Figure 17. Process to estimate the zero energy loss position. (a) Determination of the material-independent FWHM of the elastic peak, measured on carbon tape. (b) Fitting of the elastic peak in Ca_2RuO_4 with fixed FWHM extracted from carbon tape, considering only the excitation-free region (blue data points). The center of the fit should correspond to the zero energy loss position, so their difference must be subtracted. The shift has been exaggerated for better visibility. (c) Final fit of data at low energies. The elastic peak has been fitted separately before and was fixed during the final fitting.

4   Methods

To access more information about the sample, the data had to be processed where the corresponding methods for zero energy loss adjustment, data normalization and fitting are explained in this section. As a first step, DAWN, a data visualization and analysis software package developed at Diamond Light Source, was used to extract and preprocess the measured data. The exact application of this powerful program will not be further elaborated here though, but can be appreciated in Appendix A.

4.1   Zero Energy Loss

Despite many advantages of DAWN, the determination of the zero energy loss position by the software was poor because it neglects the overlap of the elastic peak with the lowest energy excitation in Ca_2RuO_4. Therefore, it had to be determined and adjusted manually. First, the expected Full Width at Half Maximum (FWHM) of the elastic peak had to be derived accurately. The FWHM of the elastic peak does not depend on the material but on the energy resolution of the instrument, which means that it does not have to be determined on our sample. Fortunately, for each RIXS measurement on Ca_2RuO_4, one was performed on carbon tape to check whether the incident beam shifts in energy over time. Amorphous carbon has a clean elastic peak which is not disturbed by any low energy features as visible in Figure 17a, hence it can be used to determine the FWHM. Thus, the data of all carbon spectra were fitted with a Voigt profile over a constant background, and their

27

estimated parameters were then averaged since they did not fluctuate much. This yields an energy resolution of

$$
\begin{array}{ll}
\text{Gaussian:} & \sigma = 0.83 \pm 0.06 \text{ meV} \\
\text{Lorentzian:} & \gamma = 0.46 \pm 0.05 \text{ meV}
\end{array}
\quad \Longrightarrow \quad
\underline{\text{FWHM} = 24.9 \pm 1.5 \text{ meV}}
$$

which can be further used in the quasi elastic fit on Ca_2RuO_4. There, assuming that the width just estimated is fixed, we can again fit the elastic peak with a Voigt profile, where position, amplitude, and constant background are free parameters yet to be determined. To include as little overlap from excitations as possible, only the data points to the left of the elastic peak maximum and the first to the right were included in the fit. For elastic scattering, the incoming and outgoing beam have the same energy which means that there is zero energy loss to the system. Therefore, the centre of the elastic fit should correspond to the zero energy loss position and needs to be subtracted otherwise, see Figure 17b.

4.2 Normalization

In order to roughly compare the intensity of an excitation for different momenta and light polarizations, the data was normalized. At the $K-$edge of the apical and planar oxygen, dd excitations are well pronounced and appear to be hardly dependent on polarization and angle θ, such that they could be used to normalize their spectra. To do so, the integral over a fixed energy range including the dd excitation, as visualized by the shaded regions in Figure 13a, was set equal to one. The dd excitations at the two distinct oxygen edges differ in shape as well as in energy, such that they were normalized over a slightly different energy region. In fact, the dd excitations disperse in energy for varying incident photon energy and their transition probability changes, meaning that dd normalization was not applicable for energy maps such as those in Figure 16. In such cases, the spectra were divided by the amplitude of the associated elastic fit. As you may have noticed, these approaches are based on rough assumptions that have their origin in visual comparison by eye. Therefore, it is appropriate to emphasize that none of the data evaluations made depend on intensity, which means that normalization has no influence on the results at all. It is used exclusively for the qualitative comparison of the different spectra.

4.3 Low Energy Fitting Procedure

The next step was to fit the low energy excitations at about 40 and 80 meV, which were approximated with two Gaussians whose parameters were not

restricted by any means. For this purpose, the elastic contribution was previously fixed such that the observations were controlled as little as possible. On top of that, an additional Gaussian has been implemented on the right to respect contributions from higher excitations. An example of such a fit can be appreciated in Figure 17c. This procedure then allows to extract the energies of the excitations which are relevant to track their dispersions discussed in Section 5.3.

4.4 350 meV Fitting Procedure

By choosing LH polarization of the incident beam whose energy was tuned to the planar oxygen absorption edge, three overlapping excitations around 350 meV could be observed. A fit with two Gaussians and one asymmetric Gaussian on the high energy side, as depicted in Figure 18a-c, reproduced the various shapes of the spectra quite well. The intensities of each of these excitations vary for different in-plane momenta, with their energy positions (see Figure 18d) being constant within their uncertainties. Calculating then the weighted mean of their energy positions over the different momenta yields the averaged energies

$$\bar{E}_2 = 276 \pm 5 \text{ meV} \qquad \bar{E}_3 = 347 \pm 5 \text{ meV} \qquad \bar{E}_{4/5} = 419 \pm 6 \text{ meV}$$

When switching polarization to LV for the same absorption edge as in Figure 22b, these features at 350 meV were still observed, but much less intensely so that the distinct peaks could not be resolved separately anymore. The fitting range of the energy positions have been weakly restricted to keep the total fit below the data that were not used for the fit. The restrictions on the three distinct widths were chosen slightly stronger, since the FWHM were expected to remain the same while changing the momentum. Still, it has to be mentioned that none of the parameters hits the boundaries of its fitting range such that one can still speak of a free fit. No restrictions on the amplitudes were made.
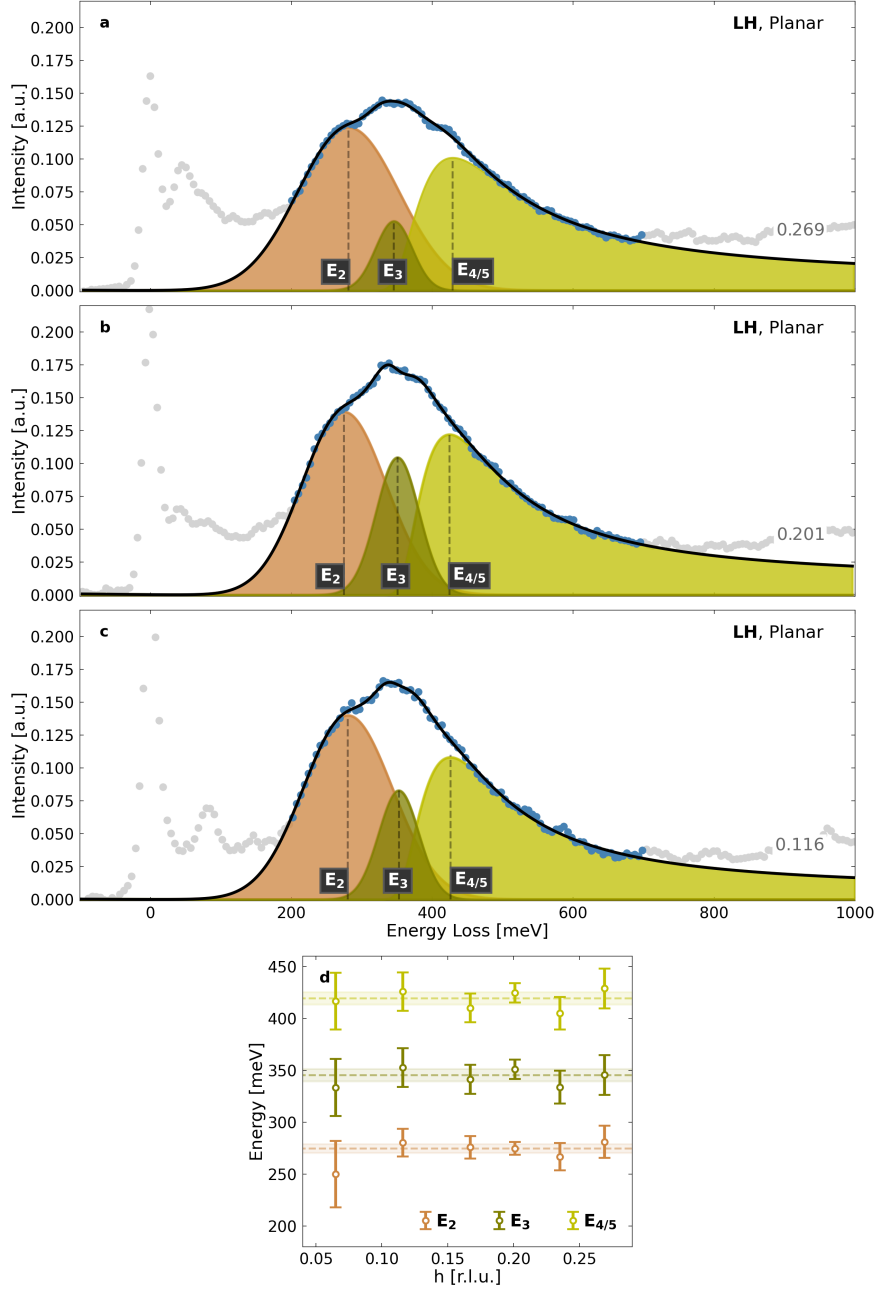
Figure 18. Visualization of the steps to estimate spin-orbit coupling λ and crystal field splitting δ. (a)-(c) Fitting of the data around 350 meV (blue data points) with two Gaussians (brown and darkgreen) and one asymmetric Gaussian (lightgreen) at higher energies. (d) Fitted energies for various in-plane momenta. The dashed lines correspond to their weighted mean value and the shaded area represents its error.

5   Discussion

Here we discuss and interpret the processed data to gain more insight into the material Ca_2RuO_4. The main focus was on the evaluation of the momentum dispersions of the excitations as well as the implementation of the theoretical model, which allows the estimation the crystal field splitting and the spin-orbit coupling. However, with interpretation comes uncertainty, meaning that the following information may have a subjective character despite all care taken.

5.1   XAS

The spectral shapes agree well with previous experiments, provided they coincide in terms of temperature, polarization and incident beam [23, 25, 34]. For comprehension, it is convenient to relate now the oxygen absorption edges to the corresponding d orbitals by following the procedure introduced previously in Section 2.2.4. The chemical description of ruthenium in an octahedral oxygen environment can be expressed as [Kr] $4d^4 5s^0$ yielding four valence electrons. Due to the additional distortion along the $c-$axis, the d_{xy} state is energetically lowered compared to the other t_{2g} states and is completely occupied. Therefore, this orbital is inaccessible through neither XAS nor RIXS and consequently does not correspond to any of the resonances observed in Figure 12. Still, the remaining two degenerate t_{2g} states $d_{xz/yz}$ can be probed and lie at lower energies than both e_g states. Hence, it is possible to assign the lower resonance at 527.3 eV (528.0 eV) to the t_{2g} state d_{xz} ($d_{xz/yz}$), where this state is accessible over its hybridization with the $2p_x$ ($2p_z$) of the apical (planar) oxygen. Or in a more compact way, the resonance at 527.3 eV belongs to the apical oxygen and the one at 528.0 eV to the planar oxygen. To conclude, the e_g states can then be associated to the remaining resonances.

5.2   Overview

To initiate a brief overview before discussion, the appearance of the excitations is summarized in Figure 19. With this, it is quite simple to see that at both absorption edges, the same excitations occur for LV polarization and for LH polarization at normal incidence. However, it seems to be reasonable since in these cases the p_x and p_y hybridizations are accessed such that due to the crystal symmetry along x and y, the same behaviour can be expected. Also, this is in accordance with the degenerate energy levels d_{xz} and d_{yz}. Comparing now the detected excitations to previous RIXS studies

32

	Apical Oxygen			Planar Oxygen		
	LV	**LH** normal	**LH** grazing	**LV**	**LH** normal	**LH** grazing
	d_{yz}	d_{xz}	d_{z^2}	$d_{x^2-y^2}$	$d_{x^2-y^2}$	$d_{xz/yz}$
40 meV	yellow	yellow	yellow	yellow	yellow	green
80 meV	green	green	yellow	yellow	yellow	yellow
160 meV	green	green	red	red	red	red
350 meV	yellow	yellow	yellow	green	green	green
750 meV	yellow	yellow	red	red	red	red

Legend: green = Clearly visible; yellow = Slightly visible/Shoulder; red = Not visible

Figure 19. Overview of the excitation occurrences under various conditions.

at the oxygen $K-$edge [23, 25], the measured excitations are also present in this study and under the same conditions. For the 350 meV though, no momentum dispersion but a substructure of at least three peaks has been resolved, whose intensities vary. In addition, an excitation at 40 meV for LH at the planar edge was detected for the first time with RIXS, and a further excitation at 160 meV for LV and LH normal at the apical edge was observed for the first time at all. The 750 meV excitation was observed at the apical oxygen $K-$edge for LH normal incidence as well as LV polarized light. Still, it could not be observed at the apical edge for LH polarized light with grazing incidence, but this could also be due to the lack of intensity.

5.3 Dispersions

With the data analysis on the low energy excitations from Section 4.3, it is now possible to discuss the momentum dispersion of the 40 and 80 meV excitations presented in Figure 20. Although an energy increase could be detected for the 40 meV excitation away from the zone center, the calculated errors are so large that this relation could also be constant within its uncertainties, rendering any interpretation meaningless. The 80 meV excitation, on the other hand, is highly dispersive and shows an energy decrease of roughly 10 meV already at a quarter of the Brillouin zone. Also, the dispersion shows no difference between LV and LH polarization of the light. The exact origin of the 80 meV excitation is somewhat debatable though. Usually in this energy range, phonons would be likely to be detected. But this assignment is unlikely since the dispersion near the zone center is rather big
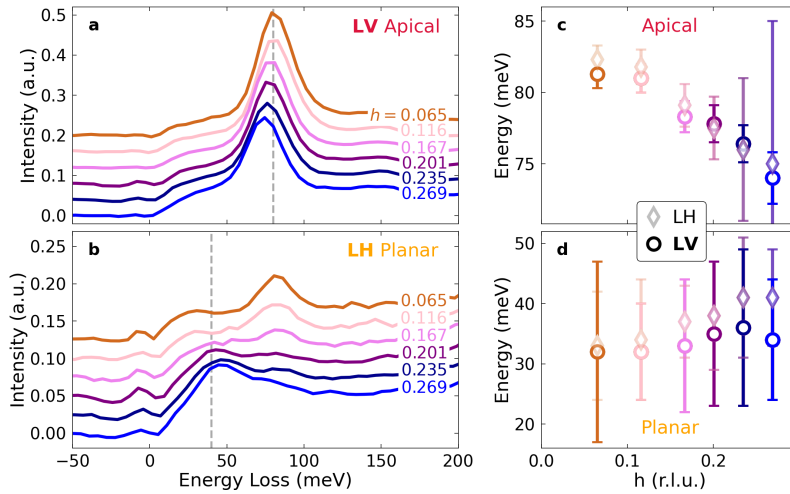
Figure 20. Visualization of the dispersing 40 and 80 meV excitations. (a)-(b) Spectra with different in-plane momentum h, shifted vertically for better comparison where the elastic peak has been subtracted. (c) Dispersion of the 80 meV excitation and (d) of the 40 meV excitation.

for optical phonons. Also supporting this exclusion is the fact that extrapolation of the present dispersion relation towards the zone center yields an excitation energy clearly above 80 meV where Raman spectroscopy detected an optical phonon just below 80 meV [35]. But still, these features lie close in energy. So to confirm that they are two distinct excitations, the phonon dispersion would have to be determined, for example by neutron scattering, and compared to the 80 meV dispersion of this thesis. Another plausible interpretation would suggest the 80 meV excitation to be of magnetic origin. In a previous paper, this low energy feature has then been connected to a two-Higgs mode [25].

5.4   Spin-Orbit Coupling and Crystal Field Splitting

Without going into detail, it is convenient to briefly introduce the theoretical model that has been used to interpret the data. This model considers the interaction terms at the ruthenium and oxygen sites as well as the kinetic term for the ruthenium-oxygen connectivity. Complete Coulomb interaction for the t_{2g} electrons, the spin-orbit coupling and the tetragonal crystal field potential have been respected for the construction of the local ruthenium Hamiltonian. Also, ruthenium-oxygen hopping contributions along the $x-$ and $y-$direction have been added. Some manipulations and derivations, which are omitted here, then diagonalize this Hamiltonian and yield the

energy Eigenvalues

$$A_1: \quad E_{A_1} \quad = \quad \tfrac{1}{2}\left(\delta - \lambda - \sqrt{\delta^2 - 2\delta\lambda + 9\lambda^2}\right)$$

$$A_{2/3}: \quad E_{A_{2/3}} \quad = \quad \tfrac{1}{2}\left(\delta - \sqrt{\delta^2 + 4\lambda^2}\right)$$

. . . .

$$B_1: \quad E_{B_1} \quad = \quad \delta - \lambda$$

$$B_2: \quad E_{B_2} \quad = \quad \tfrac{1}{2}\left(\delta - \lambda + \sqrt{\delta^2 - 2\delta\lambda + 9\lambda^2}\right)$$

$$B_{3/4}: \quad E_{B_{3/4}} \quad = \quad \tfrac{1}{2}\left(\delta + \sqrt{\delta^2 + 4\lambda^2}\right)$$

$$B_{5/6}: \quad E_{B_{5/6}} \quad = \quad \delta + \lambda$$

with crystal field splitting δ and spin-orbit coupling λ. These energy levels can be grouped in two distinct blocks A and B. This differentiation is motivated since for vanishing spin-orbit coupling $\lambda \to 0$, the values of these blocks converge to two distinct values. The A block collapses to zero, with the B block becoming equal to the crystal field splitting δ. However, the excitations that can be observed in a RIXS measurement do not belong to these energy levels. The promotion of an electron from the ground state to a higher state requires an energy equal to the level difference, such that the resulting excitation energies can be expressed as follows

$$E_1\left(\delta, \lambda\right) \quad \equiv \quad E_{A_{2/3}} - E_{A_1} \quad = \quad \tfrac{1}{2}\left(\lambda + \sqrt{\delta^2 - 2\delta\lambda + 9\lambda^2} - \sqrt{\delta^2 + 4\lambda^2}\right)$$

. . . .

$$E_2\left(\delta, \lambda\right) \quad \equiv \quad E_{B_1} - E_{A_1} \quad = \quad \tfrac{1}{2}\left(\delta - \lambda + \sqrt{\delta^2 - 2\delta\lambda + 9\lambda^2}\right)$$

$$E_3\left(\delta, \lambda\right) \quad \equiv \quad E_{B_2} - E_{A_1} \quad = \quad \sqrt{\delta^2 - 2\delta\lambda + 9\lambda^2}$$

$$E_4\left(\delta, \lambda\right) \quad \equiv \quad E_{B_{3/4}} - E_{A_1} \quad = \quad \tfrac{1}{2}\left(\lambda + \sqrt{\delta^2 - 2\delta\lambda + 9\lambda^2} + \sqrt{\delta^2 + 4\lambda^2}\right)$$

$$E_5\left(\delta, \lambda\right) \quad \equiv \quad E_{B_{5/6}} - E_{A_1} \quad = \quad \tfrac{1}{2}\left(\delta + 3\lambda + \sqrt{\delta^2 - 2\delta\lambda + 9\lambda^2}\right)$$

and are listed with increasing energy. The fitting process from section 4.4 then allowed to assign the energies E_2, E_3, and E_4 (with overlap from E_5) to the observed excitations. This interpretation is reasonable since the asymmetry could result from a weak contribution of the excitation at E_5 to the
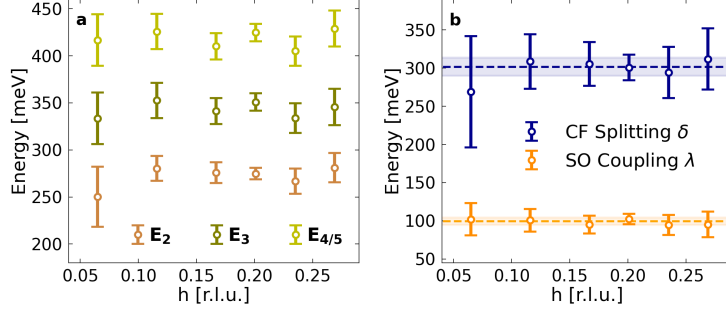
Figure 21. Determination of crystal field splitting δ and spin-orbit coupling λ. (a) Fitted energies as a function of in-plane momentum h and (b) the resulting parameters plotted against in-plane momentum h. The dashed lines correspond to their weighted mean value and the shaded areas represent the corresponding uncertainties.

dominant excitation at E_4, but it must be mentioned that other features could support or even cause such a behaviour as well. With that in mind, this approach enables the calculation of two fundamental parameters, namely the crystal field splitting δ and the spin-orbit coupling λ

$$\delta = \sqrt{\frac{E_2}{2}\left(E_3 - E_2\right)} + 2E_2 - E_3$$
$$\lambda = \sqrt{\frac{E_2}{2}\left(E_3 - E_2\right)}$$

by solving the equations of the excitation energies E_2 and E_3 for δ and λ, respectively.[3] The excitation energies were estimated by the fitting procedure such that the crystal field splitting and the spin-orbit coupling could be derived for various in-plane momenta as illustrated in Figure 21b. Both parameters do not disperse within their uncertainties, such that their weighted mean values could be calculated, resulting in

$$\bar{\delta} = 303 \pm 12 \text{ meV}$$
$$\bar{\lambda} = 99 \pm 5 \text{ meV}$$

---

[3]First, replace E_3 in the expression of E_2 and solve for the crystal field splitting δ

$$E_2 = \frac{1}{2}\left(\delta - \lambda + \sqrt{\delta^2 - 2\delta\lambda + 9\lambda^2}\right) = \frac{1}{2}\left(\delta - \lambda + E_3\right)$$

$$\implies \delta = \lambda + 2E_2 - E_3$$

Solving now the expression of E_3 for the spin orbit-coupling λ while replacing δ with the
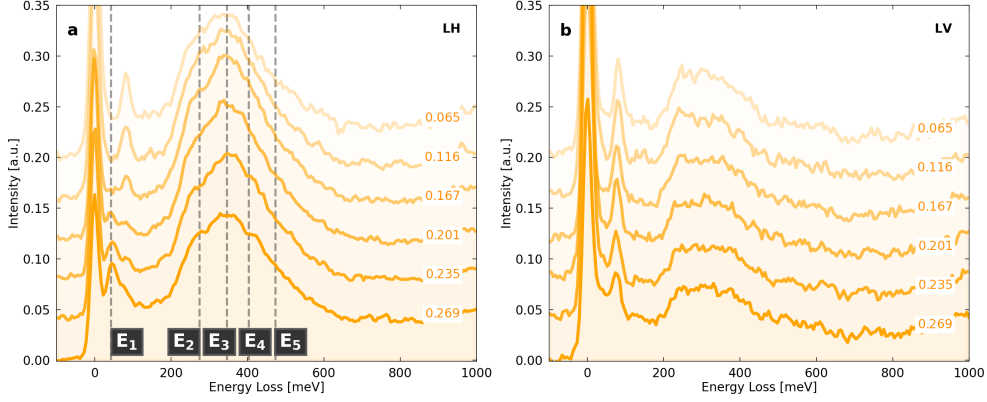
Figure 22. 350meV excitation at the planar edge for (a) LH polarization and (b) LV polarization. The vertical dashed lines represent the expected excitation energies from the theoretical model after implementing the estimated spin-orbit coupling λ and crystal field splitting δ.

These parameters agree quite well with the recent RIXS measurements at the ruthenium $L-$edge where an excellent fit was obtained for $\delta = 250$ meV and $\lambda = 130$ meV [22]. Also in Sr_2RuO_4, which is a superconducting material quite similar to Ca_2RuO_4, spin-orbit coupling has been determined to be $\lambda = 130 \pm 30$ meV [36], matching the derived value of this work within their uncertainties. Remarkably, only two of five spin-orbital excitation energies were required to determine spin-orbit coupling λ and crystal field splitting δ with this model. Nevertheless, these energies had to be assigned to the correct peaks in the RIXS spectra and left some room for interpretation, since not all expected excitations could be resolved. Therefore, it is reasonable to check whether the approach is consistent, which was done by calculating all excitation energies with the parameters δ and λ just estimated. Putting them

expression above yields

$$\implies 0 = \delta^2 - 2\delta\lambda + 9\lambda^2 - E_3{}^2 =$$
$$= \left(\lambda + 2E_2 - E_3\right)^2 - 2\left(\lambda + 2E_2 - E_3\right)\lambda + 9\lambda^2 - E_3{}^2 =$$
$$= 8\left(\lambda^2 - \frac{E_2}{2}\left(E_3 - E_2\right)\right)$$

$$\implies \lambda = \sqrt{\frac{E_2}{2}\left(E_3 - E_2\right)}$$

into the corresponding formula gives

$E_1 = 42$ meV, $E_2 = 274$ meV, $E_3 = 346$ meV, $E_4 = 403$ meV, $E_5 = 473$ meV

whose values correspond to the vertical dashed lines in Figure 22a for visualization. Comparing these results to the initial assumption that the excitation at E_4 overlaps with a weak excitation at E_5, one finds them in good agreement. Remarkably, this approach also predicts the 40 meV excitation that has been observed under these conditions. Still, it has to be stressed that this only shows consistency and needs to be examined further.

6   Conclusion and Outlook

A high resolution (FWHM $\approx$ 25 meV) oxygen $K-$edge RIXS study on Ca_2RuO_4 has been performed at the I21 beamline of the Diamond Light Source, agreeing with previous data while revealing new insight into this compound. Low energy excitations could be detected around 40, 80, 160, 350 and 750 meV that showed strong dependence on incident light polarisation. The substructure of the 350 meV excitation was assigned to inter t_{2g} transitions where theoretical modelling then suggested four distinct energy levels in this energy range, determined by crystal field splitting δ and spin-orbit coupling λ. Through data analysis, these fundamental parameters could be estimated resulting in $\delta = 303 \pm 12$ meV and $\lambda = 99 \pm 5$ meV agreeing with previous estimations. Moreover, this theory predicts a further excitation around 40 meV which was actually observed in the present study, proving consistency, and could thus be assigned to inter t_{2g} transitions. However, this is only a support but not a confirmation of the model, so further research is needed. Also, no dispersions of the inter t_{2g} excitations could be resolved for the given uncertainties. For the 80 meV excitation, a magnetic origin seems reasonable, consistent with the Higgs mode reported in Raman and neutron scattering studies [24, 35]. To exclude with certainty a phonon interpretation of the 80 meV excitation though, one would have to determine the dispersion relation of the phonon observed just below 80 meV to see whether the dispersions coincide or not. This could be achieved for example by neutron scattering. The 160 meV excitation only occurs in combination with the 80 meV excitation and is double in energy such that a connected origin seems convenient. One possible relation is given by the interpretation of the 160 meV excitation as a magnon mode with multiple spin flips. The low intensities of the 750 meV excitation accessed over the oxygen $K-$edges appear to be obstructive such that alternative methods might be more suitable to analyse these features. In previous direct RIXS measurements at the ruthenium $L-$edge for example, higher intensities were achieved already [22]. There on the other hand, the energy resolution would have to be improved to draw any further conclusions.
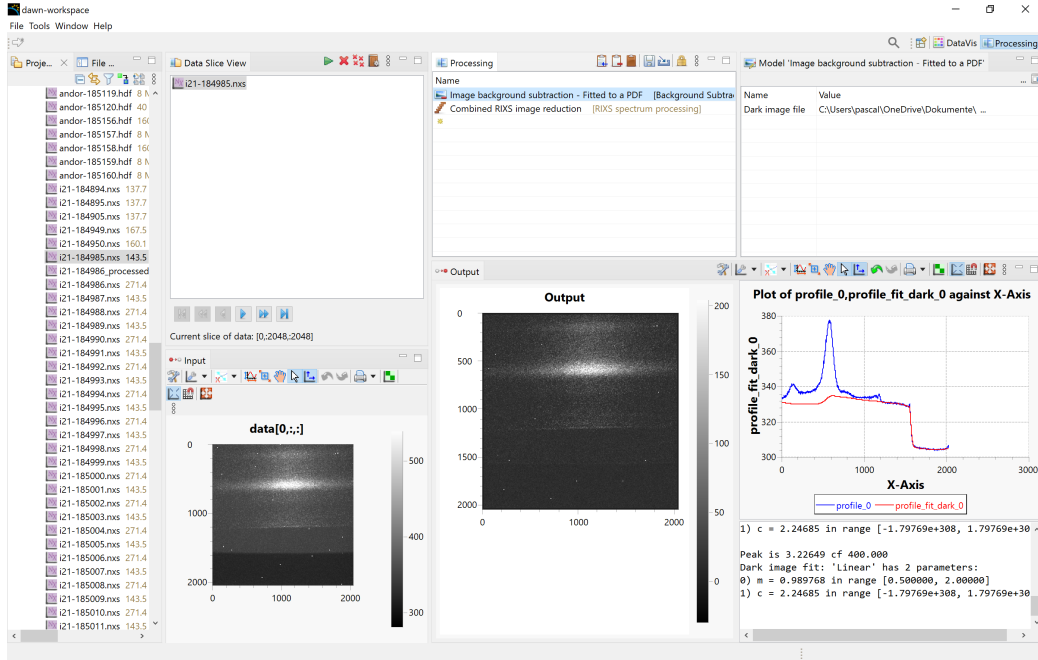
7   Acknowledgements

Figure 23. Image Background Subtraction in DAWN

Appendix

A   DAWN

With DAWN, short for Data Analysis WorkbeNch, it was possible to subtract background noise, reduce the intensity map on the detector to one RIXS spectrum and convert pixels to energy loss. In addition, this software also allowed cosmic ray peaks to be detected and subtracted, so that many processing steps were executed automatically by predefined algorithms. Here, an example of the software application will be given based on data from the present study. The DAWN workspace is divided into several panels to separate the different processing steps. To begin with, the data files to be processed must be selected in the "Project Explorer" and dragged into the "Data Slice View" panel. Those are the files that will be treated with the algorithms listed in the "Processing" panel. It turned out to be convenient to process only few files at once since processing takes some time and errors may occur. For the sample Ca_2RuO_4, the algorithms "image background subtraction" and "combined RIXS image reduction" were executed only.
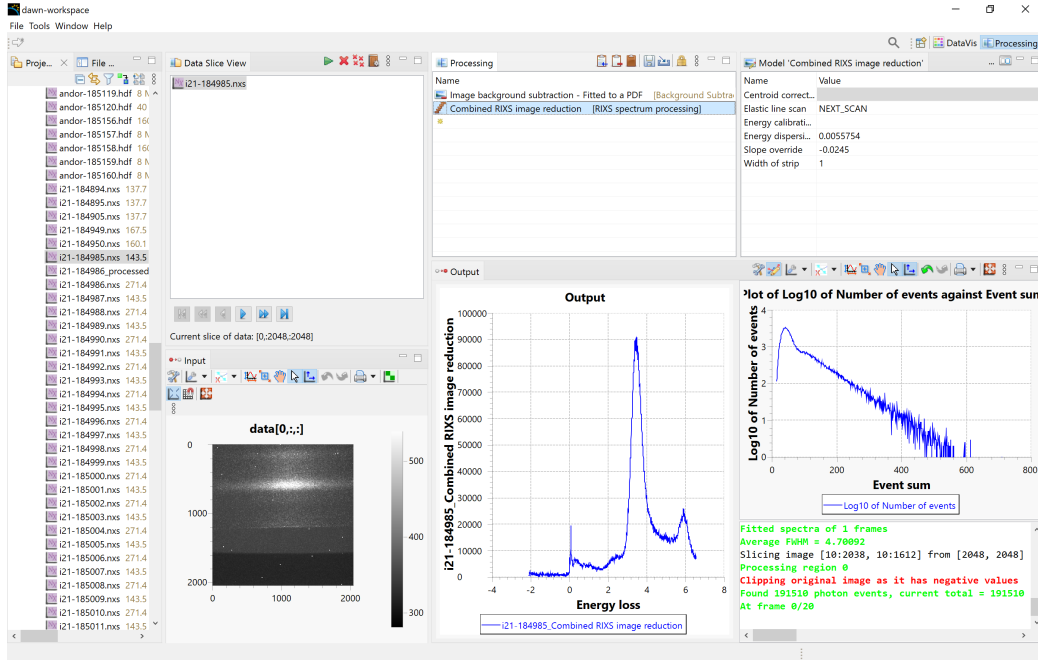
Figure 24. Combined RIXS Image Reduction in DAWN

Image Background Subtraction - Fitted to a PDF

Ambient noise is inevitable during a RIXS measurement, so it has to be subtracted subsequently. This can be achieved by measuring a dark image where no x-ray beam is incident on the sample. Then, the measured background can be subtracted from the actual data by simply selecting the dark image file in the algorithm modelling panel as done in Figure 23. Also, the output panel shows an estimation of the background subtracted intensity map whereas the background noise is displayed in the bottom right panel in red.

Combined RIXS Image Reduction

As already discussed in section 2.2.2, the RIXS intensity distribution is measured on a two-dimensional detector and needs to be reduced into one single spectrum, which this algorithm is capable of. Simultaneously, it converts the pixel to an energy loss scale and may remove random peaks caused by cosmic rays from the spectrum.

In this study, the energy dispersion was 0.0055754 eV/Pixel and is required in the algorithm modelling panel to change from pixels to an eV energy scale, see Figure 24. The slope of the elastic peak line on the detector was -0.0245
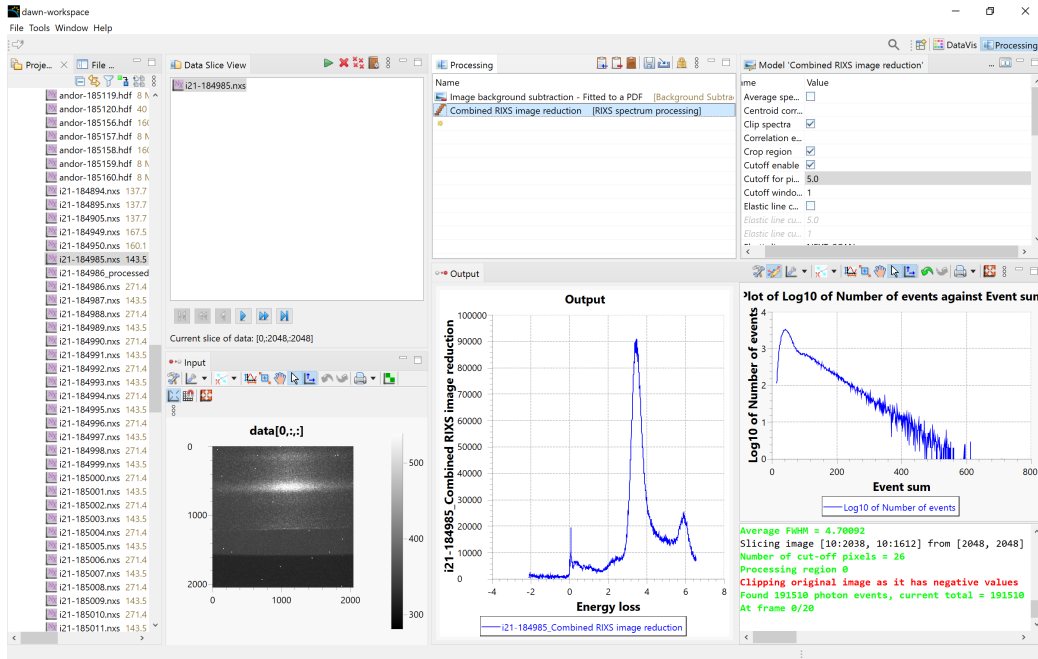
Figure 25. Cosmic Spikes subtraction in DAWN

and is needed for the correct reduction of the RIXS intensity map into one spectrum. This value can be implemented over the "Slope override" slot. The subtraction of cosmic rays is switched off by default and has to be activated manually. Pressing the "..." button located on the right top and setting a tick at the slot "Cutoff enable" activates this feature and is controlled by the value in the slot "Cutoff for pixels", as displayed in Figure 25. The smaller the values, the more aggressive is the cut off. Care must be taken, however, as values that are too small could cut off sharp features such as the elastic peak. For the present data, a value of 5.0 has turned out to be reasonable. The output panel in Figure 25 then shows an estimation of the Combined RIXS Image Reduction for these inputs.

Finally, by hitting the green triangular button, the execution of the listed algorithms in the processing panel then produce well prepared spectra that can be used for the further analysis of the data.

References

[1] C. N. R. Rao, "Transition metal oxides," *Annual Review of Physical Chemistry*, vol. 40, no. 1, pp. 291–326, 1989.

[2] J. G. Bednorz and K. A. Müller, "Possible high T_c superconductivity in the Ba–La–Cu–O system," *Zeitschrift für Physik B Condensed Matter*, vol. 64, no. 2, pp. 189–193, 1986.

[3] A. Schilling, M. Cantoni, J. Guo, and H. Ott, "Superconductivity above 130 K in the Hg–Ba–Ca–Cu–O system," *Nature*, vol. 363, no. 6424, pp. 56–58, 1993.

[4] E. Dagotto, "Complexity in strongly correlated electronic systems," *Science*, vol. 309, no. 5732, pp. 257–262, 2005.

[5] N. F. Mott, "The basis of the electron theory of metals, with special reference to the transition metals," *Proceedings of the Physical Society. Section A*, vol. 62, no. 7, p. 416, 1949.

[6] S. Jin, T. H. Tiefel, M. McCormack, R. Fastnacht, R. Ramesh, and L. Chen, "Thousandfold change in resistivity in magnetoresistive La-Ca-Mn-O films," *Science*, vol. 264, no. 5157, pp. 413–415, 1994.

[7] Y. Murakami, J. Hill, D. Gibbs, M. Blume, I. Koyama, M. Tanaka, H. Kawata, T. Arima, Y. Tokura, K. Hirota, *et al.*, "Resonant x-ray scattering from orbital ordering in $LaMnO_3$," *Physical review letters*, vol. 81, no. 3, p. 582, 1998.

[8] S. Acharya, D. Dey, T. Maitra, and A. Taraphder, "Quantum criticality associated with dimensional crossover in the iso-electronic series $Ca_{2-x}Sr_xRuO_4$," *Journal of Physics Communications*, vol. 2, no. 7, p. 075004, 2018.

[9] O. Friedt, M. Braden, G. André, P. Adelmann, S. Nakatsuji, and Y. Maeno, "Structural and magnetic aspects of the metal-insulator transition in $Ca_{2-x}Sr_xRuO_4$," *Physical Review B*, vol. 63, no. 17, p. 174432, 2001.

[10] P. Steffens, O. Friedt, P. Alireza, W. G. Marshall, W. Schmidt, F. Nakamura, S. Nakatsuji, Y. Maeno, R. Lengsdorf, M. M. Abd-Elmeguid, *et al.*, "High-pressure diffraction studies on Ca_2RuO_4," *Physical Review B*, vol. 72, no. 9, p. 094104, 2005.

[11] S. Nakatsuji and Y. Maeno, "Switching of magnetic coupling by a structural symmetry change near the mott transition in $Ca_{2-x}Sr_xRuO_4$," *Physical Review B*, vol. 62, no. 10, p. 6458, 2000.

[12] P. Steffens, O. Friedt, Y. Sidis, P. Link, J. Kulda, K. Schmalzl, S. Nakatsuji, and M. Braden, "Magnetic excitations in the metallic single-layer ruthenates $Ca_{2-x}Sr_xRuO_4$ studied by inelastic neutron scattering," *Physical Review B*, vol. 83, no. 5, p. 054429, 2011.

[13] C. Dietl, S. Sinha, G. Christiani, Y. Khaydukov, T. Keller, D. Putzky, S. Ibrahimkutty, P. Wochner, G. Logvenov, P. Van Aken, *et al.*, "Tailoring the electronic properties of Ca_2RuO_4 via epitaxial strain," *Applied Physics Letters*, vol. 112, no. 3, p. 031902, 2018.

[14] F. Nakamura, M. Sakaki, Y. Yamanaka, S. Tamaru, T. Suzuki, and Y. Maeno, "Electric-field-induced metal maintained by current of the mott insulator Ca_2RuO_4," *Scientific reports*, vol. 3, no. 1, pp. 1–6, 2013.

[15] R. Okazaki, Y. Nishina, Y. Yasui, F. Nakamura, T. Suzuki, and I. Terasaki, "Current-induced gap suppression in the mott insulator Ca_2RuO_4," *Journal of the Physical Society of Japan*, vol. 82, no. 10, p. 103702, 2013.

[16] C. Sow, S. Yonezawa, S. Kitamura, T. Oka, K. Kuroki, F. Nakamura, and Y. Maeno, "Current-induced strong diamagnetism in the mott insulator Ca_2RuO_4," *Science*, vol. 358, no. 6366, pp. 1084–1087, 2017.

[17] M. Braden, G. André, S. Nakatsuji, and Y. Maeno, "Crystal and magnetic structure of Ca_2RuO_4: Magnetoelastic coupling and the metal-insulator transition," *Physical Review B*, vol. 58, no. 2, p. 847, 1998.

[18] C. Alexander, G. Cao, V. Dobrosavljevic, S. McCall, J. Crow, E. Lochner, and R. Guertin, "Destruction of the mott insulating ground state of Ca_2RuO_4 by a structural transition," *Physical Review B*, vol. 60, no. 12, p. R8422, 1999.

[19] S. Nakatsuji, S.-i. Ikeda, and Y. Maeno, "Ca_2RuO_4: New mott insulators of layered ruthenate," *Journal of the Physical Society of Japan*, vol. 66, no. 7, pp. 1868–1871, 1997.

[20] C. G. Fatuzzo, "Spectroscopic studies of the electronic structure in layered cuprates and ruthenates," p. 183, 2017.

[21] V. Anisimov, I. Nekrasov, D. Kondakov, T. Rice, and M. Sigrist, "Orbital-selective mott-insulator transition in $Ca_{2-x}Sr_xRuO_4$," *The European Physical Journal B-Condensed Matter and Complex Systems*, vol. 25, no. 2, pp. 191–201, 2002.

[22] H. Gretarsson, H. Suzuki, H. Kim, K. Ueda, M. Krautloher, B. J. Kim, H. Yavaş, G. Khaliullin, and B. Keimer, "Observation of spin-orbit excitations and hund's multiplets in Ca_2RuO_4," *Phys. Rev. B*, vol. 100, p. 045123, Jul 2019.

[23] C. G. Fatuzzo, M. Dantz, S. Fatale, P. Olalde-Velasco, N. E. Shaik, B. Dalla Piazza, S. Toth, J. Pelliciari, R. Fittipaldi, A. Vecchione, N. Kikugawa, J. S. Brooks, H. M. Rønnow, M. Grioni, C. Rüegg, T. Schmitt, and J. Chang, "Spin-orbit-induced orbital excitations in Sr_2RuO_4 and Ca_2RuO_4: A resonant inelastic x-ray scattering study," *Phys. Rev. B*, vol. 91, p. 155104, Apr 2015.

[24] A. Jain, M. Krautloher, J. Porras, G. Ryu, D. Chen, D. Abernathy, J. Park, A. Ivanov, J. Chaloupka, G. Khaliullin, *et al.*, "Higgs mode and its decay in a two-dimensional antiferromagnet," *Nature Physics*, vol. 13, no. 7, pp. 633–637, 2017.

[25] L. Das, F. Forte, R. Fittipaldi, C. G. Fatuzzo, V. Granata, O. Ivashko, M. Horio, F. Schindler, M. Dantz, Y. Tseng, D. E. McNally, H. M. Rønnow, W. Wan, N. B. Christensen, J. Pelliciari, P. Olalde-Velasco, N. Kikugawa, T. Neupert, A. Vecchione, T. Schmitt, M. Cuoco, and J. Chang, "Spin-orbital excitations in Ca_2RuO_4 revealed by resonant inelastic x-ray scattering," *Phys. Rev. X*, vol. 8, p. 011048, Mar 2018.

[26] K. von Arx, F. Forte, M. Horio, V. Granata, Q. Wang, L. Das, Y. Sassa, R. Fittipaldi, C. G. Fatuzzo, O. Ivashko, Y. Tseng, E. Paris, A. Vecchione, T. Schmitt, M. Cuoco, and J. Chang, "Resonant inelastic x-ray scattering study of $Ca_3Ru_2O_7$," *Phys. Rev. B*, vol. 102, p. 235104, Dec 2020.

[27] K.-J. Zhou, A. Walters, M. Garcia-Fernandez, T. Rice, M. Hand, A. Nag, J. Li, S. Agrestini, P. Garland, H. Wang, *et al.*, "I21: an advanced high-resolution resonant inelastic x-ray scattering beamline at diamond light source," *Journal of Synchrotron Radiation*, vol. 29, no. 2, 2022.

[28] D. Sutter, *Bifold Insulating Energy Scales in the Mott-insulator Ca_2RuO_4: An Angle Resolve Photoemission Spectroscopy Study*. PhD thesis, Universität Zürich, 2016.

[29] R. Gross and A. Marx, *Festkörperphysik.* De Gruyter, 2018.

[30] L. J. P. Ament, M. van Veenendaal, T. P. Devereaux, J. P. Hill, and J. van den Brink, "Resonant inelastic x-ray scattering studies of elementary excitations," *Rev. Mod. Phys.*, vol. 83, pp. 705–767, Jun 2011.

[31] D. Sutter, *Strong electron correlations in the ruthenates: a spectroscopic study of Ca_2RuO_4 and $Ca_{1.8}Sr_{0.2}RuO_4$.* PhD thesis, University of Zurich, 2019.

[32] M. Schmidt, T. Cummins, M. Bürk, D. Lu, N. Nücker, S. Schuppler, and F. Lichtenberg, "Nature of the electronic states in the layered perovskite noncuprate superconductor Sr_2RuO_4," *Physical Review B*, vol. 53, no. 22, p. R14761, 1996.

[33] D. J. Singh, "Relationship of Sr_2RuO_4 to the superconducting layered cuprates," *Physical Review B*, vol. 52, no. 2, p. 1358, 1995.

[34] T. Mizokawa, L. Tjeng, G. Sawatzky, G. Ghiringhelli, O. Tjernberg, N. Brookes, H. Fukazawa, S. Nakatsuji, and Y. Maeno, "Spin-orbit coupling in the mott insulator Ca_2RuO_4," *Physical Review Letters*, vol. 87, no. 7, p. 077202, 2001.

[35] S.-M. Souliou, J. Chaloupka, G. Khaliullin, G. Ryu, A. Jain, B. Kim, M. Le Tacon, and B. Keimer, "Raman scattering from higgs mode oscillations in the two-dimensional antiferromagnet Ca_2RuO_4," *Physical Review Letters*, vol. 119, no. 6, p. 067201, 2017.

[36] C. N. Veenstra, Z.-H. Zhu, M. Raichle, B. M. Ludbrook, A. Nicolaou, B. Slomski, G. Landolt, S. Kittaka, Y. Maeno, J. H. Dil, I. S. Elfimov, M. W. Haverkort, and A. Damascelli, "Spin-orbital entanglement and the breakdown of singlets and triplets in Sr_2RuO_4 revealed by spin- and angle-resolved photoemission spectroscopy," *Phys. Rev. Lett.*, vol. 112, p. 127002, Mar 2014.